Targeting p16^{INK4a} reverses alveolar epithelial cell dysfunction and induces lung regeneration in emphysema

Bruno Ribeiro-Baptista (1, 2, 3)*, Marylène Toigo (1)*, Grégoire Justeau (1), Perla Abou-Atmeh (1), Thalles de Freitas Castro (1), Maéva Zysman (1, 4), Charlotte Thibaut De Menonville (1), Etienne Audureau (1, 5), Klara Schnyder (6, 8), Huijuan Wang (6, 7, 8), Yan Hu (9), Melanie Königshoff (9), Sophie Lanone (1), François Chabot (2, 3), Elodie Zana-Taïeb (1), Claude Jourdan Le Saux (10), Mareike Lehmann (12, 13, 14), Jean-Yves Thuret (15), Geneviève Derumeaux (1, 16), Jorge Boczkowski (1), Janine Gote-Schniering (6, 8, 11)#*, Laurent Boyer (1, 16)#*

1. Université Paris Est Créteil (UPEC), FHU SENCODE, IMRB, INSERM, Créteil, France
2. Département de Pneumologie, CHRU NANCY, Vandœuvre-lès-Nancy, France
3. Université de Lorraine, INSERM, UMR_S 1116, DCAC, Vandœuvre-lès-Nancy, France
4. Centre de Recherche cardio-thoracique de Bordeaux, U1045, Université de Bordeaux, Pulmonary Department, Centre Hospitalier Universitaire (CHU), Bordeaux, France
5. Department of Public Health, Hôpitaux Universitaires Henri Mondor, AP-HP, Créteil, France
6. Department of Rheumatology and Immunology, Inselspital, Bern University Hospital, University of Bern, Switzerland
7. Graduate School for Cellular and Biomedical Sciences, University of Bern, Switzerland
8. Lung Precision Medicine (LPM), Department for BioMedical Research (DBMR), University of Bern, Bern, Switzerland
9. Division of Pulmonary, Allergy, Critical Care, and Sleep Medicine, Department of Medicine University of Pittsburgh, Pittsburgh, PA, USA.
10. Department of Medicine, Division of Pulmonary, Critical Care, Allergy, and Sleep Medicine, University of California San Francisco, San Francisco, California, USA.
11. Department of Pulmonary Medicine, Allergology and Clinical Immunology, Inselspital, Bern University Hospital, University of Bern, Switzerland
12. Institute for Lung Research, Philipps-University Marburg, Member of the German Center for Lung Research (DZL), Marburg, Germany.

13. Comprehensive Pneumology Center (CPC), Institute of Lung Health and Immunity, Helmholtz Zentrum München, Member of the German Center for Lung Research (DZL), Munich, Germany
14. Institute for lung health (ILH), Giessen, Germany.
15. CEA, CNRS, Institute for Integrative Biology of the Cell (I2BC), Université Paris-Saclay, Gif-sur-Yvette cedex, France.
16. Département de Physiologie-Explorations Fonctionnelles, Hôpitaux Universitaires Henri Mondor, AP-HP, Créteil, France

* These two authors participated equally to this work.

shared correspondence

Keywords: regeneration, p16^{INK4a}, epithelial cells, emphysema

Abstract

Pulmonary emphysema involves impaired regenerative capacity of alveolar type 2 epithelial cells (AT2), the main progenitor cells in alveoli. However, the mechanisms underlying dysfunctional epithelial repair remain unclear. In a mouse model of elastase-induced emphysema, we observed an accumulation of activated AT2s in the lung, associated with an overexpression of p16^{INK4a} (p16), a cell cycle inhibitor known to influence stem cell fate. Deletion of p16 promoted the transition of AT2 into alveolar type 1 (AT1) cells, resulting in tissue regeneration in both mice and alveolar organoids. Pharmacological targeting of the p16 pathway using senolytic agents recapitulate this regenerative effect, further supporting the role of p16 as a key brake on epithelial plasticity. These findings demonstrate that alveolar epithelial cell dysfunction can be reversed by p16 deletion or by eliminating p16^{+} cells, thereby reactivating the AT2-to-AT1 transition and promoting endogenous alveolar regeneration. This work identifies the p16 pathway as a promising therapeutic target for restoring damaged alveoli in emphysema.

Introduction

Pulmonary emphysema is a major component of chronic obstructive pulmonary disease (COPD) characterized by progressive destruction of alveoli and is a leading cause of irreversible chronic respiratory failure. Because no current therapy can restore the alveolar architecture, identifying the mechanisms that enable regeneration of the lung structure in patients with emphysema is of critical importance.

Damaged tissues are repaired by progenitors that are activated during injury. In the alveolar epithelium, a tissue with relatively low renewal capacity, alveolar type 2 epithelial cells (AT2) are one of the main alveolar epithelial progenitor cells, which proliferate and differentiate into alveolar type 1 epithelial cells (AT1)[1]. Recent studies have revealed substantial heterogeneity within the alveolar epithelium, identifying distinct subpopulations of AT2 and intermediate transitional states that orchestrate regeneration[2–4]. AT2 stem cell dysfunction, characterized by impaired progression through these transitional states toward mature AT1, can arise from the combined effects of aging, cumulative environmental insults and genetic predisposition. This dysfunction initiates maladaptive cascades and contributes to the pathogenesis of several alveolar diseases, most notably pulmonary fibrosis[2,5–7]. However, whether similar defects in transitional epithelial populations underlie the impaired regenerative response in emphysema remains poorly understood.

A subset of these transitional epithelial states, particularly Krt8^{+} alveolar differentiation intermediates (ADI), exhibit an upregulation of senescence-associated genes including *Cdkn2a,* which encodes the cell cycle inhibitor p16^{INK4a} (p16). In emphysema, prior evidence has implicated AT2 in an apoptosis - proliferation imbalance skewed toward apoptosis [8], along with increased expression of senescent markers [9,10]. We previously demonstrated in a neonatal disease model that deletion of p16 or ablation of p16 positive cells promoted the recruitment of lipofibroblasts within the AT2 stem cell niche and enhanced alveolar regeneration from early life into adulthood[11]. However, whether targeting p16 in alveolar epithelial cells can similarly restore the regenerative capacity in adult-onset diseases such as emphysema remains unknown.

Here, we hypothesize that epithelial stem cell dysfunction is a key driver of the persistent alveolar destruction in emphysema and that targeting p16 could restore regeneration in the diseased lung. Using an elastase-induced mouse model of emphysema together with human and mouse-derived alveolar organoids, we found that alveolar epithelial stem cell dysfunction

87 marked by p16 overexpression, and accumulation of activated AT2 cells characterized by
88 elevated expression of *Lcn2* and *Lrg1,* contributed to emphysema pathogenesis by impairing
89 lung regeneration. Genetic deletion of p16 reversed this dysfunction, reduced activated AT2
90 accumulation, and restored alveolar regeneration *in vivo* and in organoid cultures. Moreover,
91 pharmacological clearance of p16^{+} senescent cells using senolytic agents also restored
92 epithelial function and ameliorated emphysema. Together, our findings identify p16-driven
93 epithelial stem cell dysfunction as a central mechanism of emphysema progression and
94 establish targeting p16^{+} cells as a potential regenerative therapeutic strategy in chronic lung
95 disease.

96 Results

97 Alveolar epithelial stem cell dysfunction in elastase-induced emphysema is characterized 98 by an increase in activated AT2 cells

99 To assess whether emphysema alters epithelial progenitor capacity, we employed a murine
100 model in which a single intratracheal instillation of elastase produces persistent alveolar injury.
101 This model recapitulated hallmark features of emphysema, including persistent airspace
102 enlargement, as evidenced by a significant and sustained increase in mean linear intercept
103 (MLI) from day 21 through day 150 post-injury (**Fig. 1A–C**).

104 We first evaluated whether the irreversible structural damage observed *in vivo* reflects a defect
105 in the intrinsic regenerative capacity of epithelial progenitors. To this end, EpCAM^{+} epithelial
106 cells were isolated from control and emphysematous lungs and cultured in organoids with
107 primary lung fibroblasts. Notably, epithelial cells from emphysematous lungs generated
108 significantly fewer and smaller organoids than controls, both at day 14 and 21 of culture (**Fig.
109 1D–E, Supplementary Fig. 1A**), indicating that emphysema is associated with a durable
110 reduction in epithelial regenerative capacity.

111 To determine whether these alterations are conserved in humans, we isolated primary AT2
112 cells by magnetic sorting of HT2-280^{+} cells from explanted lungs of emphysematous and non-
113 emphysematous patients (**Fig. 1F, Supplementary Fig. 1B**) and co-cultured them with
114 primary fibroblasts derived from independent donors (both emphysematous and non-
115 emphysematous). To interrogate the potential relationship between organoid formation and
116 clinical features, we performed an exploratory unsupervised (clustering) analysis using the
117 Kohonen's self-organized map (SOM) methodology[12], including the following parameters for

118 both AT2 and fibroblasts patients: number and size of the organoids, age, level of smoking
119 (pack-years), CT scan emphysema score[13] and lung function parameters (FEV1, FEV1/FVC,
120 DLCO). We observed that organoids were fewer and smaller if AT2 came from
121 emphysematous patients compared to controls based on emphysema score and lung function
122 parameters (DLCO, FEV1) (**Fig. 1F**). However, we did not observe an overlap between
123 organoid size and number with the fibroblast characteristics, suggesting that emphysematous
124 AT2 may be the main driver of organoid formation variation (**Supplementary Fig.1C**). This
125 was further substantiated in paired AT2-fibroblast organoid co-cultures, where
126 emphysematous and non-emphysematous derived AT2 cells were co-cultured with the
127 fibroblasts of the same donor (**Fig. 1G-H**). Emphysematous AT2 yielded significantly fewer
128 organoids than their non-emphysematous AT2 counterparts (n = 18 pairs**, Fig. 1G-H**).
129 Collectively, these data demonstrate that AT2 cell dysfunction is a conserved feature of
130 emphysema in both mice and humans.

131 To uncover the cellular and molecular programs underlying this defective epithelial
132 regeneration, we next performed single-cell RNA sequencing (scRNA-seq) of lung epithelial
133 cells from control and emphysematous mice. FACS-sorted $CD31^{-}CD45^{-}EpCAM^{+}$ cells were
134 profiled at day 21 and day 150 post-elastase or PBS treatment, corresponding to early and
135 chronic phases of emphysema (**Fig. 1I, Supplementary Fig. 1D-F**). After quality control, we
136 recovered 31,172 high-quality epithelial transcriptomes spanning all major alveolar and airway
137 epithelial subtypes (AT2, proliferating AT2, AT1, club, goblet, and ciliated cells)
138 (**Supplementary Fig. 1G, Supplementary Table 1**).

139 Within the alveolar compartment, subclustering of $Sftpc^{+}$ cells revealed three transcriptionally
140 distinct AT2 populations: (i) canonical AT2 cells expressing classical markers (*Sftpc, Etv5,*
141 *Cxcl15*), (ii) a subset of AT2 cells characterized by *Lrg1*, *Lcn2*, and *Il33* expression, and (iii)
142 a subset defined by *Areg*, *Krt8*, and *Lgals3* expression (**Fig. 1J–L, Supplementary Table 2**).
143 These two last AT2 subpopulation exhibited transcriptional similarity to previously described
144 activated/primed AT2[3,4,14] and $Krt8^{+}$ transitional alveolar differentiation intermediates
145 (ADI)s/regenerative AT2 cells/DATP/PATS respectively[2–4,6,15,16], two alveolar epithelial cell
146 states that transiently emerge during specific stages of lung regeneration after fibrotic injury.
147 The similarity of these two subpopulations with activated AT2 and ADI was supported by
148 matchSCore analysis with respective cell state marker genes from a bleomycin-induced lung
149 fibrosis scRNA-seq dataset (**Supplementary Fig. 1I**)[14,17]. Notably, in contrast to
150 ADI/PATS/DATP cells described in fibrosis, these cells retained AT2 identity and were also

151 present in control lungs. We therefore designated this subset as pre-ADI to distinguish it from
152 fully transitional populations. Compositional analysis revealed a selective expansion of
153 activated AT2 cells in emphysematous lungs. Their abundance was increased at day 21 and
154 further enriched by day 150, whereas pre-ADI populations remained unchanged (**Fig. 1M,**
155 **Supplementary Fig. 1H**).

156 To ensure that this observation was not restricted to the elastase model, we performed
157 independent validation using external datasets. In a publicly available scRNA-seq dataset of
158 mice exposed to cigarette smoke for six months[18], we also observed a significant enrichment
159 of our activated AT2 cell signature (**Fig. 1N**). Importantly, projection of the mouse gene
160 signature onto two independent human COPD single-cell datasets[18,19] confirmed a
161 reproducible accumulation of activated AT2 cells in emphysematous lungs (**Fig. 1O)**.
162 Altogether these results suggest that alveolar epithelial dysfunction, characterized by an
163 accumulation of activated AT2 cells is an important feature of emphysema.

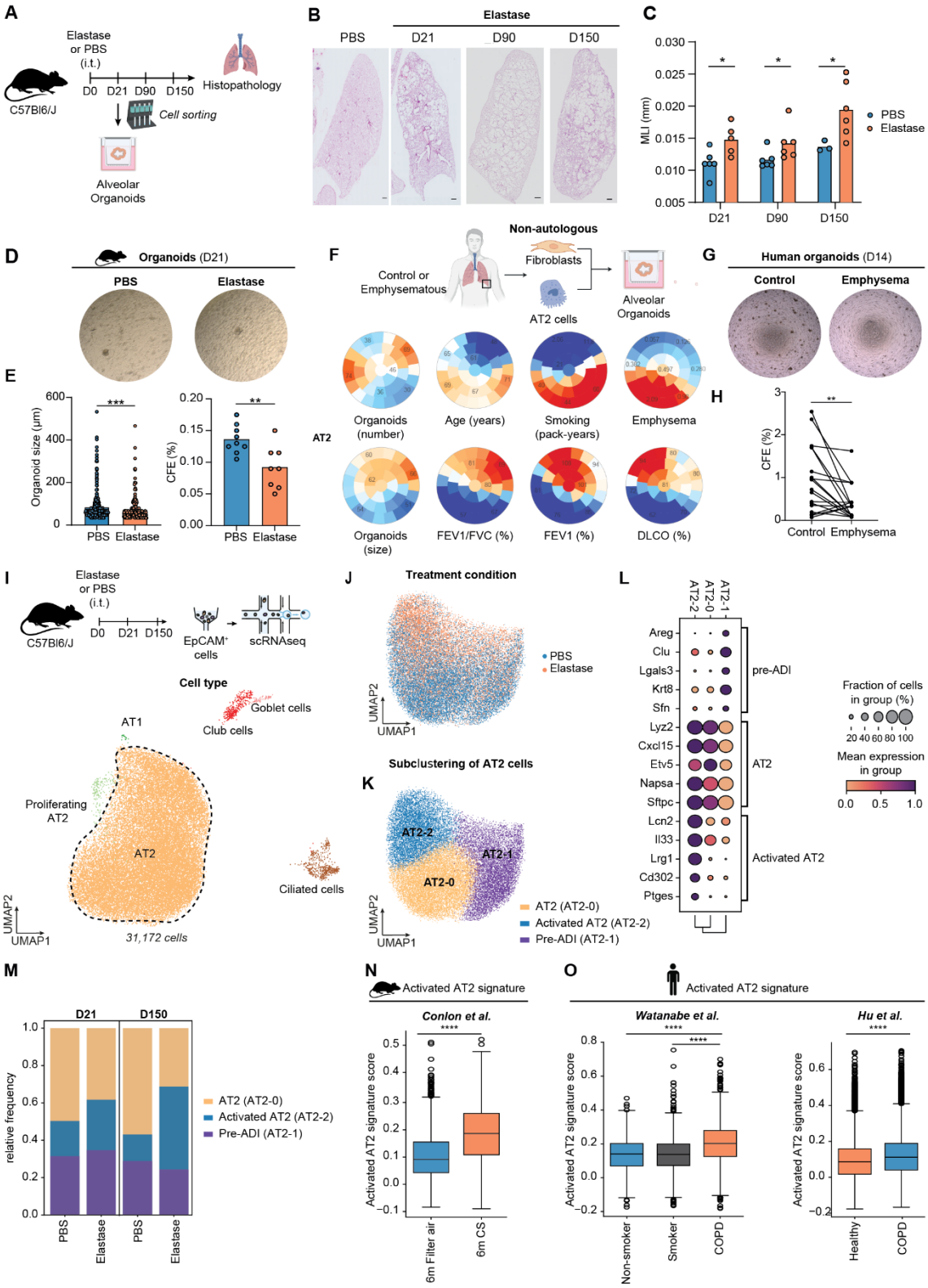

Figure 1: Alveolar epithelial dysfunction and accumulation of activated AT2 in mouse emphysema (A) Experimental design for lung histopathological analysis and organoid formation assays using isolated lung epithelial cells (EpCAM^{+}CD45^{-}CD31^{-}) from the elastase-induced emphysema mouse model. (B) Representative hematoxylin and eosin stainings of lungs at D21, D90 and D150 post-treatment of elastase or PBS (scale bar = 500 µm). (C) Quantification of mean linear intercept (MLI) measurements (mean is shown, N = 3-6 per group, Mann Whitney test at each time point). (D) Representative images of organoids obtained from co-culture of EpCAM^{+} cells from elastase- or PBS-treated mice with wildtype (WT) fibroblasts after 21 days of culture. (E)

Quantification of the colony forming efficiency (CFE, %) and organoid size (μm) (mean is shown, N = 8/group, n > 200 organoids/group, Mann-Whitney test). (F) Exploratory unsupervised analysis of the number and size of formed organoids, patient age, smoking history (in pack-years), proportion of emphysema as quantified by chest computed tomography, FEV_1/FVC ratio (%), FEV_1 (%), and DLCO (%) of human alveolar organoid assays using AT2 from control or emphysematous patients (n=16) and primary fibroblasts from control or emphysematous patients from different donors (n=8). Color intensity reflects the standardized (z-score) value of each variable, allowing visual comparison across patient subgroups, blue represents the lowest average values, and red the highest. Abbreviations: FEV_1/FVC ratio (forced expiratory volume in 1 second / forced vital capacity), FEV_1 (forced expiratory volume in 1 second), FVC (forced vital capacity), DLCO (diffusion capacity of the lung for carbon monoxide). (G) Representative images of human alveolar organoids formed at day 14. (H) CFE as a function of AT2 cell origin. Each data point corresponds to a co-culture of primary fibroblasts with AT2 cells from a patient without emphysema, compared to the culture of the same fibroblasts with AT2 cells derived from emphysematous tissue (N = 18, Wilcoxon matched pairs signed rank test). (I) **S**ingle-cell RNAseq from isolated epithelial cells ($EpCAM^+CD45^-CD31^-$) of mouse lungs from elastase-induced emphysema model at day 21 and day 150**.** Uniform manifold approximation and projection (UMAP) showing the cell type annotation. (J) UMAP of AT2 cells clustering depending on PBS or elastase treatment. (K) UMAP of Leiden subclustering of AT2 cells. (L) Dotplot of the marker gene signature of the different AT2 subpopulations. (M) Relative frequency of AT2 subpopulations depending on treatment and timepoint. (N, O) Scoring of the gene signature of the murine activated AT2 cells applied to independent emphysema datasets, including: Conlon et al.[18] (mouse lungs exposed to six months of filtered air or cigarette smoke, and O Watanabe et al.[19] (non-smoker, smoker, and COPD patients), and Hu et al.[20](healthy vs COPD patients). *p = 0.05, **p = 0.01, ***p = 0.001, ****p = 0.0001 and ns = not significant

Alveolar epithelial stem cell dysfunction in elastase-induced emphysema is associated with p16 overexpression.

Having established that emphysema is characterized by a shift in AT2 cell state composition, we next sought to define the molecular programs within the AT2 lineage that might underlie their impaired regenerative potential. Differential gene and pathway analyses of the total AT2 population (*Sftpc*$^+$ cells) from elastase and PBS-treated mice revealed a marked and persistent transcriptional reprogramming at both early (day 21) and chronic (day 150) stages (**Fig. 2A–B**, **Supplementary Fig. 2A-B, Supplementary Tables 3 and 4**). Elastase treatment induced a shift toward inflammatory and immune-regulatory pathways, including an increase of TNF-α, IL-1β and IL-4/IL-13 signaling, and type I and II interferon responses, signaling axes previously shown to modulate AT2 progenitor function and contribute to maladaptive epithelial repair in chronic lung diseases, including COPD[3,21–23]. Consistent with these pathway changes, many of the top elastase-responsive genes corresponded activated AT2 markers, including *Lcn2*, *Lrg1*, *Cxcl17*, *Cd14*, and members of the uPAR family *Ly6a* and *Ly6i*. Notably, transcriptional regulators of activated AT2 and AT2-to-AT1 differentiation, such as *Tfcp2l1* and epithelial β1-integrin, were not prominently modulated[24,25]. In addition, elastase also altered expression of cell-cycle–related genes, including *Ccnd2* and *Cdca7*, with early induction of *Fos* and *Fosb*, suggesting disrupted proliferative control. Consistent with these

observations, signatures of cyclin-dependent kinase pathway dysregulation and increased cellular senescence were detected. Because these findings raised the possibility that senescence may contribute to AT2 dysfunction, we directly assessed senescence signatures within the different AT2 lineage populations. Senescence scores were highest in activated AT2 and pre-ADI cells and further increased following elastase treatment at both time points (**Fig. 2C, Supplementary Fig. 2C-D**). In parallel, expressions of cell cycle associated signatures, including E2F targets, G2/M checkpoint regulators, and mitotic spindle genes were broadly reduced across AT2 subsets (**Fig. 2D, Supplementary Fig. 2C/D**), consistent with impaired cell-cycle progression. As p16 (*Cdkn2a*) is a key regulator of stress-induced cell-cycle arrest and cellular senescence, we examined its expression in elastase-injured lungs. Although *Cdkn2a* transcripts were not detected in the scRNA-seq dataset, immunostaining revealed a marked increase in $p16^{+}$ AT2 cells at all examined time points (**Fig. 2E–F**).

Together, these findings identified p16-associated cell-cycle arrest as a potential barrier to AT2-mediated repair, prompting us to test whether p16 deletion could restore epithelial regenerative capacity in emphysema.

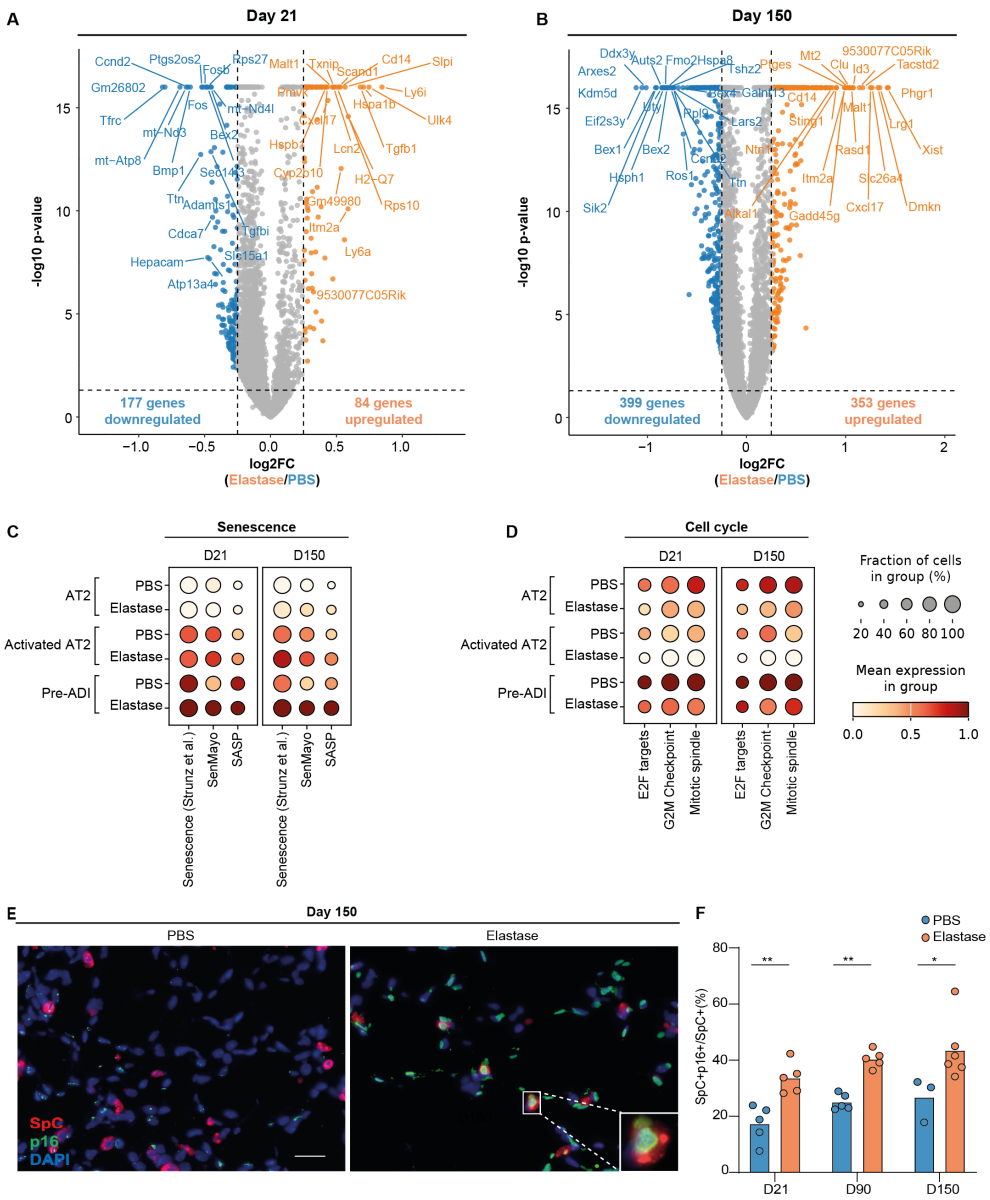

Figure 2: Alveolar epithelial stem cell dysfunction in elastase-induced emphysema is associated with p16 overexpression. Volcano plot of differentially expressed genes at D21 (A) and D150 (B) in AT2 cells of elastase-treated mice compared to PBS controls. A log fold change of 0.25 and q-value of less than 0.05 was used to define differential expressions. Upregulated genes are shown in orange, downregulated genes in blue, and non-significant genes in grey. (C) Dot plot depicting mean scores for three senescence-related gene sets (from[4,26] and (D) three MSigDB hallmark cell cycle-related gene sets (E2F targets, G2M checkpoint, Mitotic spindle) in the different AT2 subpopulations stratified by treatment condition and timepoint. (E) Representative immunofluorescence staining of pro-SpC (red) and p16 (green) in lungs from PBS and elastase-treated mice. (F) Quantification of p16^{+} AT2 cells as a proportion of total AT2 cells. Data represent mean values (N = 3–6 mice per group). Statistical significance was assessed by Mann–Whitney test at each time point. *p = 0.05, **p = 0.01, ***p = 0.001, ****p = 0.0001 and ns = not significant

p16 deletion induces alveolar regeneration and reverses epithelial stem cell dysfunction in emphysema

245 To assess whether indeed p16 overexpression contributes to impaired epithelial repair, we
246 treated WT and p16$^{-/-}$ mice with elastase and evaluated lung morphology at day 21 (established
247 emphysema), and at days 90 and 150 (persistent emphysema) post-instillation (**Fig. 3A**). At
248 day 21, airway enlargement as quantified by MLI was comparable between WT and p16$^{-/-}$
249 mice following elastase injury, indicating that p16 deficiency does not prevent initial alveolar
250 destruction (**Fig. 3B–C**). However, by day 90, p16$^{-/-}$ mice showed a significant reduction in
251 MLI, indicating spontaneous improvement of emphysema. This regeneration persisted through
252 day 150 (**Fig. 3B–C**).

253 To assess whether improved morphometric outcomes were accompanied by restored epithelial
254 progenitor function, we generated alveolar organoids using EpCAM^{+} cells isolated from WT
255 or p16$^{-/-}$ mice 21 days after elastase injury and co-cultured them with WT lung fibroblasts. P16
256 deletion significantly increased organoid number and size (**Fig. 3D-E**), indicating that p16
257 deletion restored epithelial stem cell function in emphysema. To test whether p16 deletion
258 influences epithelial progenitor potential independently of injury, EpCAM^{+} cells from PBS-
259 treated WT or p16$^{-/-}$ mice were co-cultured with WT fibroblasts. While organoid numbers were
260 unchanged, organoid size was increased in cultures with p16$^{-/-}$ cells (**Fig. 3F-G**), suggesting
261 that p16 also modulates baseline epithelial growth potential.

262 To assess whether fibroblasts contribute to p16-mediated regeneration, we generated organoids
263 using EpCAM^{+} cells from elastase-instilled mice co-cultured with fibroblasts with or without
264 p16 deletion from elastase-treated lungs. P16$^{-/-}$ fibroblasts produced only a slight, non-
265 significant increase in organoid formation, although overall organoid numbers were low
266 (**Supplementary Fig. 3A-B)**, and p16 deficiency did not increase the fibroblast proliferative
267 potential (**Supplementary Fig. 3C**). Furthermore, immunohistochemistry at day 90 showed no
268 differences in adipose differentiation-related protein (ADRP) staining across genotypes,
269 excluding a role for lipofibroblasts in the regeneration process (**Supplementary Fig. 3D–E**).

270 Together, these findings indicate that p16 deletion promotes spontaneous late alveolar
271 regeneration primarily through intrinsic epithelial mechanisms, rather than fibroblast-mediated
272 effects.

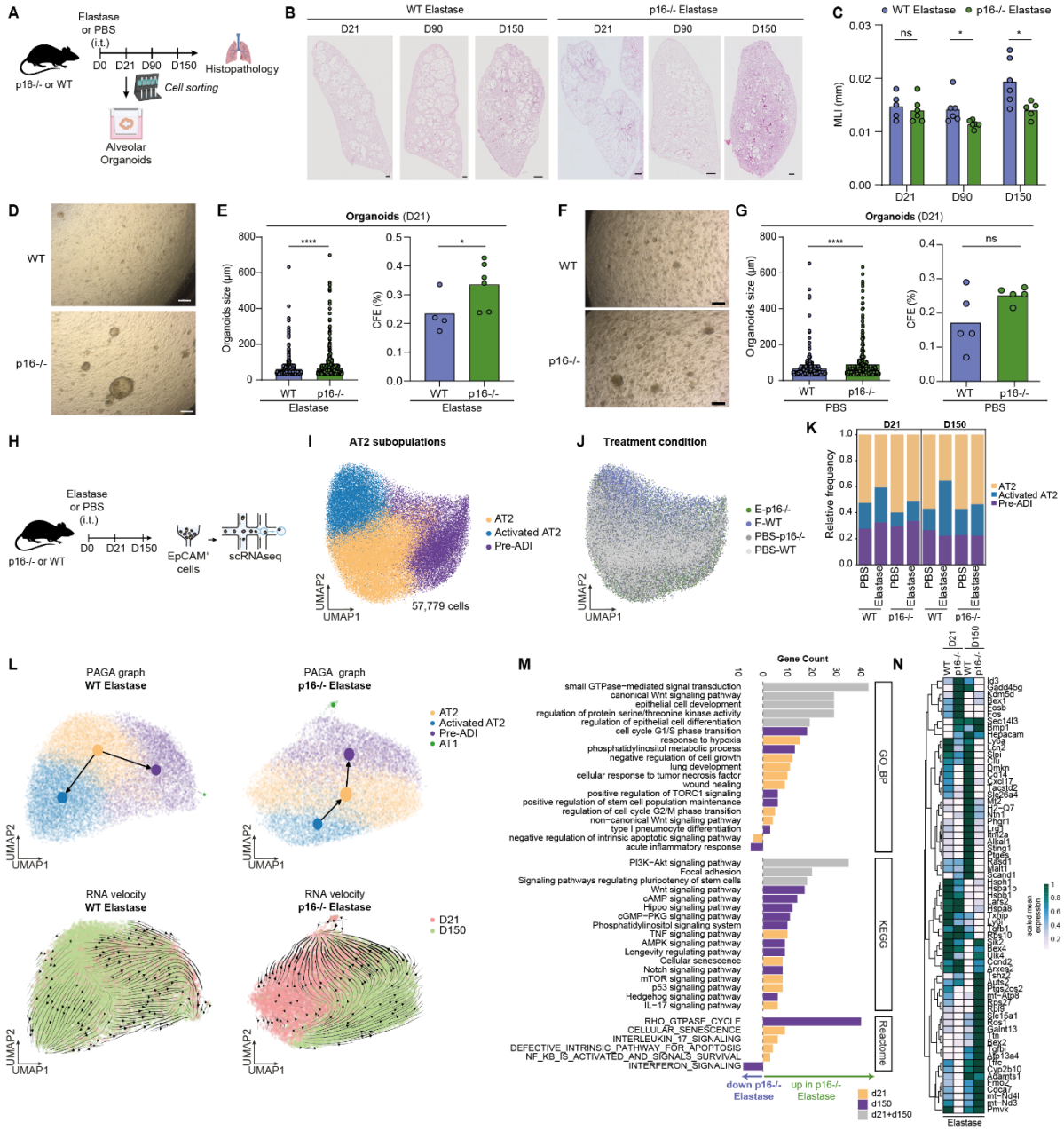

Figure 3: p16 deletion induces lung regeneration and decrease activated AT2 in elastase treated mice (A) Experimental design for lung histopathological analysis and organoid formation assays using isolated epithelial cells (EpCAM^{+}CD45^{-}CD31^{-}) from lungs of WT and p16$^{-/-}$ mice treated with elastase or PBS, respectively. (B) Hematoxylin-eosin staining of WT and p16$^{-/-}$ lungs at D21, D90 and D150 post-elastase injury (scale bar = 500 µm). (C) Quantification of mean linear intercept (MLI) (mean is shown, N = 5-6, Mann Whitney test at each time point). (D) Representative images of organoids obtained with EpCAM^{+} from WT and p16$^{-/-}$ treated with elastase after 21 days of culture (scale bar = 20 µm). (E) Size (µm) and colony forming efficiency (CFE %) of organoids obtained from EpCAM^{+} cells from WT or p16$^{-/-}$ mice treated with elastase (mean is shown, N>3/group, n > 200 organoids/group, Mann-Whitney test). (F) Representative images of organoids obtained with EpCAM^{+} from WT and p16$^{-/-}$ treated with PBS after 21 days of culture (scale bar = 20 µm). (G) Size (µm) and colony forming efficiency (CFE %) of organoids obtained from EpCAM^{+} cells from WT or p16$^{-/-}$ mice (mean is shown, N>3/group, n > 200 organoids/group, Mann-Whitney test). (H) Experimental design of scRNA-seq profiling in WT and p16$^{-/-}$ mice. (I-J) UMAP of *Sftpc*+ AT2 cells depending on cell type annotation. (K) Relative frequency of AT2 subpopulations depending on genotype, treatment, and analysis timepoint. (L) UMAPs with scVelo and PAGA results from WT or p16-/- mice treated with elastase depending on AT2 subpopulations and AT1 (upper panel) or depending on timepoints (lower panel), respectively. (M) Results of GO and pathway enrichment

290 analysis stratified by time point and pathway category comparing AT2 from WT or p16$^{-/-}$ mice treated with
291 elastase. (N) Heatmap of differential expressed genes in WT or p16$^{-/-}$ mice treated with elastase at D21 and D150.
292 *p = 0.05, **p = 0.01, ***p = 0.001, ****p = 0.0001 and ns = not significant

293

294 **Alveolar regeneration is associated with the restoration of alveolar epithelial cell**
295 **subpopulations**

296 To identify the epithelial populations responsible for the p16-dependent regenerative response,
297 we first examined cell state changes in elastase-injured WT and p16$^{-/-}$ lungs. We performed
298 scRNA-seq on EpCAM^{+}CD31^{-}CD45^{-} epithelial cells from WT and p16$^{-/-}$ mice at days 21 and
299 150 after elastase injury (**Fig. 3H**). After quality control, we recovered 59,275 epithelial cells,
300 including 57,779 AT2 cells (**Supplementary Fig. 4A)**. The previously defined AT2
301 subpopulations, i.e. canonical AT2, activated AT2, and pre-ADI cells, were preserved across
302 genotypes, treatments and timepoints (**Fig.3I-J, Supplementary Fig.4B-C**). Strikingly, p16
303 deletion markedly reduced the proportion of activated AT2 cells in elastase-injured lungs,
304 restoring their abundance to WT baseline levels at both time points (**Fig. 3K**).

305 To examine whether p16 deletion restores the AT2-to-AT1 differentiation trajectory, we
306 performed RNA velocity analysis (scVelo) and summarized lineage relationships with
307 partition-based graph abstraction (PAGA). In WT elastase-injured lungs, RNA velocity
308 predicted a differentiation trajectory of AT2 cells toward either activated AT2 or pre-ADI cells
309 in elastase-injured lungs (**Fig. 3L**), indicating a diversion into injury-associated programs with
310 limited progression toward terminal differentiation. By contrast, p16$^{-/-}$ lungs exhibited
311 trajectories consistent with effective regeneration, with activated AT2 cells progressing toward
312 canonical AT2, pre-ADI, and ultimately AT1 cells (**Fig. 3L**). These computational predictions
313 were supported by immunofluorescence analyses showing increased overall AT2 abundance
314 and expansion of regenerative SpC^{+}/KRT8^{+} intermediates in p16$^{-/-}$ lungs (Supplementary **Fig.**
315 **3F-I**).

316 To elucidate the mechanisms by which p16 deletion reduces activated AT2 cells and restores
317 regenerative capacity, we performed differential gene expression and pathway analyses
318 between elastase-treated AT2 cells from WT and p16$^{-/-}$ animals (**Fig. 3M-N, Supplementary**
319 **4D/E, Supplementary Tables 5 and 6**). By day 150, p16 loss resulted in a broad reversal of
320 the transcriptional programs induced by elastase injury. Among the top upregulated genes in
321 elastase-treated WT AT2 cells, including *Lcn2, Lrg1, Cd14, Cxcl17, Id3, Dmkn, Phgr1, Ptges,*

322 *Clu, Tacstd2*, and *Slc26a4* were strongly downregulated in elastase-treated p16$^{-/-}$ AT2 cells
323 (**Fig. 3N**). These genes are characteristic of the persistent activated AT2 state, suggesting that
324 p16 is required to sustain this maladaptive program. Conversely, several genes suppressed by
325 elastase in WT mice and associated with AT2 cell cycling, stress tolerance, and differentiation
326 capacity, such as *Ccnd2, Sik2, Auts2, Ttn, Hsph1, Hspa8,* and *Bex4* were upregulated in p16$^{-/-}$
327 AT2 cells. Together, these reciprocal changes indicate that p16 deletion shifts AT2 cells out of
328 an arrested, inflammation-driven state and back toward a regenerative trajectory.

329 Pathway analyses further supported the restoration of AT2-to-AT1 differentiation potential. In
330 p16$^{-/-}$ AT2 cells, pathways central to epithelial renewal and AT1 maturation, including Wnt
331 and Notch signaling, epithelial cell development, type I pneumocyte differentiation, and stem
332 cell pluripotency programs, were prominently enriched (**Fig. 3M**). Additionally, cell-cycle
333 pathways (e.g., G1/S and G2/M transitions) and pro-survival programs such as PI3K–Akt and
334 mTOR signaling were upregulated, consistent with the increased proliferative and regenerative
335 competence observed in p16-deficient lungs. Notably, enrichment of senescence and p53
336 signaling pathways was largely confined to day 21, suggesting that p16 deletion reshapes the
337 temporal dynamics of senescence to permit later differentiation and lineage progression.

338 Altogether, these results suggest that p16 deletion reverses elastase-induced epithelial
339 dysfunction by reducing activated AT2 cells and reactivating programs that restore AT2-to-
340 AT1 differentiation and alveolar regeneration.

341 **p16 deletion induces alveolar regeneration without aberrant process of fibrosis or cancer**

342 We next questioned if this regenerative process driven by p16 deletion could be in part aberrant
343 with the development of fibrosis or lung cancer[27]. We thus quantified septal thickness
344 (**Supplementary Fig. 5A)**, collagen deposition **(Supplementary Fig. 5B**), and myofibroblasts
345 content **(Supplementary Fig. 5C**) as markers of lung fibrosis. These markers were transiently
346 increased at D90 in p16$^{-/-}$ mice as compared to WT animals and returned to the baseline level
347 at D150, confirming the absence of an aberrant remodeling process and suggesting an important
348 step in the regenerative process involving fibrogenesis. At histological level, we did not
349 observe any pulmonary neoplastic process during the follow-up of mice with a deletion of p16
350 until D150. Moreover, a CT scan was performed 1 year after elastase instillation on the lungs
351 of WT and p16$^{-/-}$ mice. We did not observe any tumors, also excluding a long-term process of
352 lung carcinogenesis associated with p16 deletion and emphysema (**Supplementary Fig. 5D**).

P53 is a crucial tumor suppressor that suppresses lung adenocarcinoma development from AT2. At the gene level, the emphysematous destruction was associated at D21 with an elevation of p53 and p21 mRNA (**Supplementary Fig. 5E-F**). Altogether, these results show that p16 deletion triggers spontaneous alveolar regeneration in emphysema once lesions are established without the occurrence of fibrosis or lung cancer.

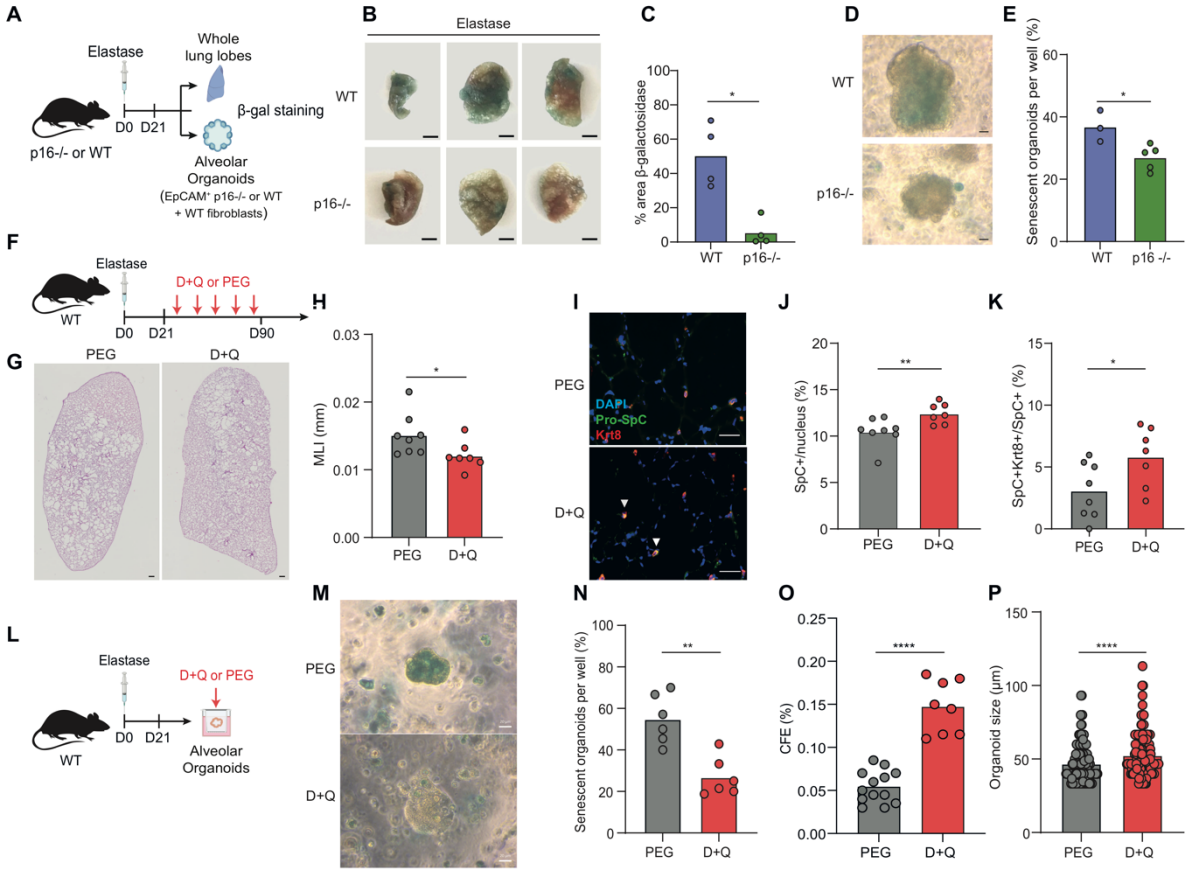

Figure 4: Elimination of senescent cells by senolytics restores epithelial function and reverses emphysema. (A) Experimental design of alveolar organoid formation with EpCAM^{+} cells from WT or p16$^{-/-}$ mice instilled with PBS or elastase cocultured with WT fibroblasts. (B) β-galactosidase activity staining of mouse lungs harvested from p16$^{-/-}$ or WT mice at D21 of elastase instillation (scale bar = 2 mm) and (C) quantification (mean is shown, N = 4/group, Mann-Whitney test). (D) Representative images of β-galactosidase activity staining on organoids (scale bar = 20 µm) and (E) quantification (mean is shown, N >3/group, Mann-Whitney test). (F) Schematic timeline of treatment with senolytics Dasatinib and Quercetin (D+Q) or PEG as control in elastase-treated WT mice. (G) Hematoxylin-eosin staining of the lung at D90 of elastase-treated mice treated with senolytics or PEG as control and (H) quantification of mean linear intercept (MLI) (mean is shown, N=7-8/group, Mann-Whitney test, scale bar = 500 µm). (I) Immunofluorescence staining of Pro-SpC (green) and KRT8 (red) at day 90. (J) Quantification of the number of AT2 cells among all cells (mean is shown, N=7-8/group, Mann-Whitney test). (K) Quantification of the number of Pre-ADI (Pro-SpC^{+}/KRT8^{+}) cells among AT2 cells (mean is shown, N=7-8/group, Mann-Whitney test). (L) Schematic of organoids treatment with D+Q or PEG from EpCAM^{+} of WT mouse lungs treated with elastase. (M) Representative images of β-galactosidase activity staining on organoids (scale bar = 20 µm) and (N) quantification of the proportion of senescent organoids (mean is shown, N=6/group, Mann-Whitney test). (O) CFE and (P) size of organoids at D14 of culture treated with D+Q or PEG. *p = 0.05, **p = 0.01, ***p = 0.001, ****p = 0.0001 and ns = not significant.

377

378 **Elimination of p16+ cells by senolytics restores epithelial function and reverses**
379 **emphysema**

380 To confirm that deletion of p16 modulates senescence in our mice model of emphysema, we
381 quantified senescence by analyzing senescence-associated βgalactosidase (SA-βgal) staining
382 in lungs from WT and $p16^{-/-}$ mice following elastase injury (**Fig. 4A**). $p16^{-/-}$ lungs showed
383 reduced SA-βgal staining at day 21 (**Fig. 4B, C**). Similarly, organoids derived from $EpCAM^{+}$
384 cells of $p16^{-/-}$ lungs had fewer SA-βgal–positive structures compared to WT (**Fig. 4D, E**).

385 To evaluate the therapeutic potential of eliminating $p16^{+}$ cells and reducing senescence, we
386 tested the senolytics Dasatinib and Quercetin in both an *in vivo* emphysema model and organoid
387 assays. WT mice with established emphysema were treated from day 21 to 90 (**Fig. 4F**).
388 Senolytic treatment significantly reduced MLI (**Fig. 4G-H**), increased AT2 cell numbers, and
389 elevated the proportion of pre-ADI cells ($SpC^{+}/KRT8^{+}$) compared to vehicle-treated controls
390 (**Fig. 4I–K**). In parallel, we treated with senolytics organoids generated by co-culturing WT
391 fibroblasts with $EpCAM^{+}$ cells from emphysematous WT lungs (**Fig. 4L**). Senolytics reduced
392 SA-βgal staining in organoids (**Fig. 4M-N**) and significantly increased both organoid number
393 and size, indicating improved epithelial progenitor function (**Fig. 4O-P**). Together, these
394 results confirm that targeting $p16^{+}$ senescent cells can restore epithelial function and promote
395 alveolar regeneration in emphysema.

396

397 **DISCUSSION**

398 In this study, we show that alveolar stem cell dysfunction in elastase-induced emphysema is
399 associated with an accumulation of activated AT2 cells and p16 overexpression. Genetic
400 deletion of p16 restores epithelial progenitor function and promotes alveolar regeneration.
401 Finally, pharmacological elimination of $p16^{+}$ cells using senolytics reverses both epithelial
402 dysfunction and emphysematous lung destruction. Collectively, these findings identify
403 activated AT2 cells as potential bottlenecks in the regenerative process and establish p16 as a
404 central regulator of their maladaptive behavior, highlighting senescence-targeted interventions
405 as a promising therapeutic avenue for emphysema.

406 In models of injury-activated lung regeneration, lineage tracing and single-cell based RNA
407 velocity analyses have revealed stage-specific AT2 intermediates that emerge along the AT2-
408 to-AT1 differentiation continuum[2–4]. Early inflammatory primed or activated AT2 populations
409 are followed by ADI/DATP/PATS transitional cells, which are now understood as essential
410 intermediates required for successful alveolar repair. Recent work by Konkimalla et al.
411 demonstrates that ablation of ADI/DATP/PATS cells causes alveolar simplification resembling
412 emphysema, whereas sustained induction of these cells promotes fibrotic remodeling[27,28]. These
413 findings suggest that roadblocks along the differentiation trajectory and imbalances in
414 transitional epithelial states can drive divergent pathological outcomes.

415 Here, using an elastase-induced emphysema model, we show that activated AT2 cells
416 aberrantly accumulate. Single-cell RNA-seq–based trajectory analyses suggest that in
417 emphysematous lung, the activated AT2 state becomes a dead-end, with minimal evidence of
418 progression toward AT1 differentiation. Strikingly, p16 deletion seems to reopen this stalled
419 trajectory, restoring differentiation toward pre-ADI and AT1 states without inducing fibrosis
420 or neoplastic changes. This aligns with our organoid findings showing improved progenitor
421 function in both injury and homeostasis contexts. These findings suggest that activated AT2
422 cells in emphysema represent a maladaptive or arrested epithelial state that potentially drives
423 lung pathology.

424 Hu *et al.* recently discovered a club-cell derived emphysema enriched AT2 subset in both
425 humans (asATII) and mice (ATII-6) with poor alveolar progenitor potential. The cells express
426 markers such as *Ly6i, Lcn2, Slc26a4, Slpi,* genes that were also upregulated in our activated
427 AT2 cell population[20]. We also found evidence of activated AT2 cell signatures in smoking
428 induced emphysema and other human COPD datasets, suggesting a conserved pathological
429 state across mice and humans.

430 The precise role of activated AT2 cells in driving emphysema progression remains to be
431 determined. Their integration within the alveolar stem cell niche, and their interactions with
432 distal airway–derived epithelial populations, remain poorly understood. It is also unclear
433 whether these cells functionally differ from analogous transitional states seen in fibrosis models
434 or represent an entirely distinct disease-specific phenotype.

435 Our data suggest mechanistic hypotheses for how p16 enforces the arrest of AT2
436 differentiation. Canonical regulators of AT2 plasticity leading to activated AT2 signatures,

437 such as YAP/TAZ, Tfcp2l1, or β1-integrin[24,25], were not significantly modulated in our single-
438 cell analyses. Instead, p16 deletion was for instance associated with a strong induction of
439 GTPase-mediated signaling pathways. GTPases are known to promote epithelial cell
440 proliferation and survival through activation of mitogenic pathways such as MAPK/ERK and
441 PI3K/AKT[29]. These pathways are essential for stem cell expansion and repair following injury.
442 In addition, GTPases integrate extracellular signals, including mechanical signals, to modulate
443 regenerative responses[30–32], positioning them as key regulators of epithelial renewal that
444 contribute to active maintenance of AT1 cell identity[32]. These findings suggest that p16
445 programs may intersect with mechanotransduction circuits, thereby imposing a differentiation
446 block on activated AT2 cells.

447 Another question is whether there are cell-extrinsic signals in the alveolar microenvironment
448 that reinforce the persistence of activated AT2 cells. The work by Konkimalla et al.[27] highlights
449 the need for precise temporal coordination between epithelial and fibroblast transitional states
450 to rebuild the fibroelastic scaffold during regeneration. In our model, we observed transient
451 accumulation of αSMA+ myofibroblasts at day 90 in $p16^{-/-}$, raising the possibility that
452 disrupted epithelial–mesenchymal balancing may contribute to the persistence of activated
453 AT2 cells or limit access to regenerative trajectories. Future studies are needed to test whether
454 emphysema disrupts these epithelial-mesenchymal crosstalk and how such disruptions feed
455 back onto epithelial fate decisions.

456 Age further modifies these interactions. We had previously demonstrated that p16 deletion or
457 elimination of $p16^{+}$ cells in the post-natal hyperoxia model of bronchopulmonary dysplasia
458 induced a catch-up alveolar growth between childhood and adulthood[11]. In that model, the
459 restoration of alveolar structure at adulthood was mainly associated with an increase in
460 lipofibroblasts adjacent to AT2 cells after p16 deletion or $p16^{+}$ cells removal. Interestingly, this
461 lipofibroblast expansion was absent in adult emphysema, indicating that the mechanisms by
462 which p16 regulates regeneration differ fundamentally between developmental and adult lungs,
463 even though the regenerative outcome of p16 removal is preserved. The age-dependent
464 divergence between these models underscores the complexity of the role of p16 across
465 developmental stages and suggests that senescence intersects with distinct stromal–epithelial
466 circuits in neonatal versus adult lungs. Nevertheless, in both models, regeneration emerges only
467 at late time points, suggesting that p16 removal resets long-term epithelial trajectories rather
468 than accelerating acute repair.

469 Finally, our senolytic experiments emphasize the translational potential of these findings.
470 Previous studies have shown that p16 is overexpressed in emphysema, both in mouse models
471 and in human[9,33,34]. Eliminating p16^{+} cells in vivo and in organoids reduces senescence burden,
472 enhances AT2 progenitor activity, increases pre-ADI intermediates, and reverses established
473 alveolar destruction. These results provide compelling evidence that senescence-targeted
474 therapies can restore regenerative capacity even in chronic, advanced emphysema.

475 In conclusion, our study highlights that targeting p16 in alveolar epithelial cells could be a
476 promising approach to regenerate the lung in emphysema without inducing an aberrant fibrotic
477 of oncogenic processes. Harnessing tissue regeneration in this context could open a novel
478 therapeutic window for patients with severe and irreversible lung disease.

479

480 # Methods

481 **Animals**

482 C57BL/6J mice (8-14 weeks, male and female) were housed in a pathogen-free barrier
483 environment throughout the study (12 h light/dark cycle with access to food and water ad
484 libitum). The Institutional Animal Care and Use Committee approved experimental procedures
485 on mice (APAFIS#25872-2020060317048060v3). The p16$^{INK4a-/-}$ mice were kindly provided
486 by Anton Berns (Netherlands Cancer Institute, Amsterdam)[35].

487 **Elastase-induced emphysema**

488 Mice were randomly assigned into PBS or elastase groups. The lung injury was induced by an
489 intra-tracheal instillation of a single dose administration of 2 UI of elastase (Elastin Products
490 Company) diluted in sterile 50 µL of PBS. The control group was treated with sterile PBS only.
491 Mice were sacrificed on day (D)21, D90 and D150 after instillation. All analyses were done
492 blinded.

493 **Lung morphometry**

494 Murine lungs were perfused with a cannula at 25 cmH2O for 30 min and fixed in 4%
495 paraformaldehyde. Next, they were embedded in paraffin and sectioned at 5 µm thickness.
496 Hematoxylin/eosin staining was performed according to standard procedures. Ten digital

497 photomicrographs at 20X magnification were performed in the histological section. To
498 evaluate the degree of pulmonary emphysema, we used the standard morphometric method of
499 the mean linear intercept as described by Knudsen L et al[36]. Collagen content was evaluated
500 after Sirius red staining as previously described[37].

501 **Senescence-associated β-galactosidase staining**

502 Senescence-associated β-galactosidase staining was performed in whole-amount lungs using
503 the Senescence β-Galactosidase Staining Kit (Cell Signaling©). Briefly, lung whole-amount
504 was fixed at room temperature for 45 min in 1 % paraformaldehyde fixative solution, washed
505 three times with PBS, and incubated overnight at 37°C with the Staining Solution containing
506 X-gal in N-N-dimethylformamide (pH 6.0). Whole lungs were subsequently dehydrated with
507 two consecutive steps in 50% and 70% ethanol and embedded in paraffin for serial sectioning.
508 Sections were counterstained with nuclear fast red.

509 **Immunofluorescence staining**

510 We prepared and stained formalin-fixed, paraffin-embedded 5-µm-thick lung sections using
511 standard procedures. Briefly, sections were deparaffinized through graded Xylene then
512 rehydrated in aqueous solutions with decreasing alcohol concentrations and washed in PBS.
513 Immunofluorescence staining was performed using anti-proSpC (Abcam, ab90716 1/500), anti
514 α-smooth muscle actin (Abcam, ab5694, 1/200), anti-KRT8 (DSBH, TROMA-I, 4 µg / mL),
515 anti-ADRP (Progen GP42, 1/400), anti-p16 (Abcam, ab54210, 1/200). Secondary antibodies
516 (Life Technologies; A11056, A11008, A11001, A11006, A11062, A11012) were incubated for
517 1 h at room temperature. Nuclei were counter-stained using prolonged anti-fade reagent with
518 DAPI (Life Technologies©, E1740384). Image acquisition was performed using a fluorescence
519 microscope (Axioimager M2; Zeiss) at X40 magnification. For quantitative analyses,
520 randomized images were taken (Axiophoto; Carl Zeiss MicroImaging equipped with a digital
521 camera AxiocamHRc; Carl Zeiss MicroImaging). The quantification of the different stainings
522 was performed using Image J.

523 **RNA extraction and gene expression analysis**

524 RNA extraction from sorted murine lung cells was done using RNeasy kit (Qiagen©) and
525 quantitative real-time PCR (*q*PCR) analysis was performed using Quant Studio 6 (Applied
526 Biosystems, Illkirch, France) Data were presented as expression relative to hypoxanthine-

527 guanine phosphoribosyl transferase 1 (Hprt 1). For qPCR, the following primers were used :
528 ink4a (fwd: GCAGTGTTGCAGTTTGAACCC; Rev: GTGGCAACTGATTCAGTTGG);
529 Tp53 (Fwd: GGCCCCTGTCATCTTTTGTC; Rev: TGGAGGTGTGGCGCTGA) ; Hprt1
530 (Fwd: GTTAAGCAGTACAGCCCCAAAATG; Rev:
531 TCAAGGGCATATCCAACAACAAAC).

532 **Mouse alveolar organoids**

533 Primary lung fibroblasts were isolated from mouse lungs after enzymatic and mechanical
534 dissociation. In brief, lungs were perfused with ice-cold PBS through the right ventricle,
535 excised and minced in small pieces that were placed in dispase (5 UI/ml, Corning), type 1
536 collagenase (Gibco, 17100-017) and placed in a Gentlemacs Octodissociator (Miltenyi) for 45
537 min at 37°C. After digestion, the solution was filtered in 70- and 40-micron strainer (Corning),
538 washed and plated in Dulbecco's Modified Eagle's Medium/F12 (Invitrogen) supplemented
539 with antibiotic/antimycotic (Thermofischer 15240062) and 10% FBS (Hyclone). Six hours
540 post-plating, supernatant with non-adhesive cells was removed. The purity of culture was
541 assessed by staining for vimentin and the absence of staining for αSMA, CD31, CD45 and
542 cytokeratin. At the 2nd passage, 50,000 fibroblasts were co-cultured with 20,000 EpCAM^{+} cells.
543 These cells were obtained by the same protocol of digestion followed by a negative (Ter119^{-}
544 CD31^{-}CD45^{-}LNGFR^{-}CD16/32^{-}CD90^{-}) than a positive magnetic bead sorting (EPCAM^{+}). Cells
545 were resuspended in SABM (small airway basal medium supplemented with vial except
546 epinephrin) and mixed with matrigel (Corning) at a ratio of 1/1 and added to 24-well transwell
547 filter inserts with 0.4 microns pores (Corning) in a 24-well tissue culture plate containing 500
548 µL of medium (SABM). The medium was supplemented with Rock inhibitor for the 48 first
549 hours then changed every 2 days. Cultures were incubated at 37°C in a humidified incubator
550 (5% CO2). The number of organoids (colony forming efficiency) and the size were analyzed
551 on day 14 and 21 post-plating.

552 **Human alveolar organoids**

553 Fibroblasts and AT2 cells were obtained from lung tissue from patients undergoing lung
554 surgery for lung cancer from Tenon Hospital, France with documented information and non-
555 opposition for the use of biological waste materials (EP-TN-TU-PLUS-ORG-DE-001).
556 Primary lung fibroblasts were isolated by the explant's technique as described previously[37].
557 Briefly, this method involves finely dissecting a small sample of pulmonary parenchyma to

558 remove pleural elements, macroscopic bronchi, and vessels. The dissected tissue is then seeded
559 in a six-well plate with suitable culture media. Over several days, fibroblasts migrate and
560 adhere to the plastic plating. After three passages, all other cell types are eliminated, leaving
561 only pulmonary fibroblasts. AT2s were obtained by magnetic bead sorting using an anti-HT2-
562 280 antibody (Terrace biotech). A suspension of 50,000 fibroblasts and 5,000 AT2 were mixed
563 with matrigel (Corning) at a ratio of 1/1 and added to 24-well transwell filter inserts with 0.4
564 µm pores (Corning) in a 24-well tissue culture plate containing 500 µL of medium (SABM,
565 Lonza). The medium was supplemented with Rock inhibitor for the first 48 hours then changed
566 every 2 days. Cultures were incubated at 37°C in a humidified incubator (5% CO2). The
567 number of organoids (colony forming efficiency) and the size were analyzed on day 14 post-
568 plating.

569 **Senolytic drug treatments**

570 Dasatinib (D) and quercetin (Q) were used *in vitro* at 5 µM and 50 µM respectively, and DMSO
571 was used as a control. For the *in vivo* experiment, senolytics were delivered by oral gavage
572 every five days at 5mg/kg for Dasatinib and 50 mg/kg for Quercetin from D21 to D90 after
573 elastase instillation in 10% propylene glycol (vehicle).

574 **Single-cell RNAseq**

575 For scRNA-seq, a single-cell suspension was prepared from the $EpCAM^{+}CD31^{-}CD45^{-}$ cells
576 (Anti-CD326: 118213 1/100, Anti-Ter119: 116208, Anti-CD31: 102418 1/100, Anti-CD45:
577 103155 1/100, DAPI: 422801 1/300, Biolegend) sorted by FACS from the lungs of 2 mice
578 pooled for each group at day 21 and 150 following PBS or elastase instillation in WT or $p16^{-/-}$
579 mice, respectively. Approximately 20,000 cells were loaded onto a 10x Genomics Chip G with
580 Chromium Single Cell 3′ v3.1 gel beads and reagents (3′ GEM v3.1, 10x Genomics). Single
581 index libraries were generated following the manufacturer's protocol (10x Genomics,
582 CG000204_RevD). The scRNA-seq libraries were pooled and sequenced using a NovaSeq
583 6000 instrument [read 1: 28 base pairs (bp), Index1 8bp/ Index2 0bp/read2 55bp]. Count
584 matrices were produced using the Cellranger computational pipeline (v7.0.1, STAR v2.7.2a),
585 with reads aligned to the mm10 mouse reference genome (GRCm38). After preprocessing and
586 quality control, scRNA-seq data were analyzed using the Python package Scanpy (> v1.8.2)
587 following the current Single Cell Best Practice Guidelines: https://www.sc-best-
588 practices.org/preamble.html.

589 **Preprocessing and analysis of epithelial cells scRNA-seq data**

590 To reduce the impact of batch correction on downstream annotations, we first processed and
591 annotated the WT mouse datasets independently, and only afterward integrated them with the
592 p16$^{-/-}$ samples. Quality metrics were calculated using scanpy *sc.pp.calculate_qc_metrics*
593 function. During quality control, genes with fewer than one count or expressed in fewer than
594 ten cells were excluded. Low quality cell filtering was performed using automatic thresholding
595 via the median absolute deviation (MAD) technique, setting 5 MADs for the
596 *log1p_total_counts, log1p_n_genes_by_counts* and *pct_counts_in_top_20_genes* fractions to
597 identify outlier cells. *pct_counts_Mt* were filtered with 5 MADs. Additionally, cells with a
598 percentage of mitochondrial counts exceeding 10 % were filtered out. Doublets were identified
599 using Scrublet[38] on each sample separately, and ambient RNA contamination was corrected
600 with soupX[39], with the contamination fraction manually set to 0.4. Normalization was
601 performed using scran's size factor approach, based on Louvain clustering (resolution = 1.0).
602 Finally, log transformation was applied with the pp.log1p() function in scanpy.

603

604 **Highly variable genes (HVGs) calculation and cell type annotations**

605 For each sample, we identified the top 4000 highly variable genes (HVGs) and considered a
606 gene as globally variable only if it was consistently variable across at least four samples. The
607 remaining HVGs were then used as input for Principal Component Analysis (PCA), followed
608 by the construction of a k-nearest neighbor (kNN) graph based on the first 50 principal
609 components. Clustering was performed using the Leiden algorithm, and clusters were
610 annotated based on canonical marker genes. Initially, we carried out a coarse annotation of the
611 dataset and then extracted the EpCAM^{+} epithelial compartment, which included both alveolar
612 and airway cell types, while filtering out contaminant cells from other cell lineages and low
613 quality cells. We then repeated HVG selection, PCA, and clustering to refine the epithelial cell
614 annotation.

615

616 **Differential gene expression testing (DGE)**

617 Differential expression analysis was carried out using diffxpy (v0.7.4). A Wald test with default
618 settings was applied to all genes detected in at least five cells. Genes were considered
619 significantly differentially expressed when they showed a log2 fold change greater than 0.25
620 and an FDR-adjusted *p*-value below 0.05.

621

622 **Gene signature scoring**

623 A gene signature for the activated AT2 cell population was derived from the WT AT2 dataset
624 based on a FDR-adjusted *p*-value < 0.05 and a log2 fold change > 2. The final set included the
625 following genes: *Scd1, Lrg1, Lcn2, Itih4, Hdc, Mfsd2a, Ptges, Cxcl17, H2-Q7,*
626 *9530077C05Rik, Proz, Phgr1, Alkal1, Slc5a1, Dmkn,* and *Fgg*. In addition, to quantify the
627 expression of senescence and cell cycle pathways, publicly available senescence lists from
628 Strunz et al.[4], Saul et al.[26] and Coppe et al.[40], and cell cycle lists from the MSigDB database
629 were retrieved. Signature scores were computed in Scanpy using the sc.tl.score_genes()
630 function (default settings), by subtracting the mean expression of randomly selected control
631 genes from the mean expression of the signature genes.
632
633 **Re-analysis of publicly available single-cell RNAseq data**
634 To assess whether the activated AT2 gene signature was also enriched in other independent
635 scRNA-seq datasets from murine and human lung emphysema, we scored our activated AT2
636 cell signature on publicly available datasets from COPD patients (GEO GSE173896[19] and GEO
637 GSE222374[20]), and cigarette smoke exposed mice (GEO GSE151674)[18]. The results were
638 tested for statistical significance using either a Kruskal-Wallis test for multiple or Mann-
639 Whitney U test for two group comparisons. In addition, to assess the transcriptional similarity
640 of the identified AT2 subpopulations with AT2 subpopulations discovered in Bleomycin-
641 induced fibrosis[41], matchScore analysis was performed as previously described[14].
642
643
644 **Gene ontology and pathway enrichment analysis**
645 Gene ontology (GO) and pathway enrichment analysis was performed in R using the
646 clusterProfiler package[42], with libraries from the KEGG, Reactome, and GO Biological
647 Processes and GO Molecular Function databases. Gene sets were considered enriched if the
648 FDR-corrected p-value was below 0.05.
649
650 **Trajectory inference analysis**
651 Trajectory inference analysis and fate mapping was conducted using the Python packages
652 scVelo (version 1.10.1) and CellRank (version 2.0.4). We inferred the splicing kinetics of all
653 genes and estimated RNA velocity using the dynamical model in scVelo. We confirmed this
654 finding by inferring the trajectory of AT2 sub-populations using Partition-Based Graph
655 Abstraction (PAGA) analysis.
656

657 **Unsupervised analysis**

658 An exploratory unsupervised (clustering) analysis was performed using the Kohonen's self-
659 organized map (SOM) methodology[12] to identify if clinical, functional, and radiological
660 characteristics of control and emphysematous patients are linked to the capacity of their AT2
661 cells or fibroblasts to form organoids. Briefly, this algorithm allows to build 2-dimensional
662 maps from multidimensional datasets, where each map is divided into small groupings
663 ('districts') in which data points (here, the co-cultures) are automatically located by the SOM
664 algorithm based on their characteristics: co-cultures with similar features are closely located
665 on the maps, while co-cultures with distinct profiles are farther from each other. Variables
666 considered for this analysis included the number and size of organoids formed, patient age (in
667 years) and gender, smoking history (in pack-years), the proportion of emphysema as quantified
668 by chest computed tomography, the FEV_1/FVC ratio (%), FEV_1 (%), and DLCO (%). The
669 SOMs were generated using the Numero R package[43] after principal component analysis
670 adapted for mixtures of qualitative and quantitative variables was applied (PCAMix)[44].

671

672 **Statistical analysis**

673 All statistical analyses were conducted using GraphPad Prism (version 10) or the scipy.stats
674 module in Python. The statistical tests used were Mann–Whitney U tests, Wilcoxon matched-
675 pairs signed rank tests, two-way ANOVA, Kruskal–Wallis tests. Data were presented as
676 mean values ± SEM, and results were considered statistically significant if $p < 0.05$.

677

678 # References

679 1. Barkauskas, C. E. *et al.* Type 2 alveolar cells are stem cells in adult lung. *J. Clin. Invest.* **123**,
680 3025–3036 (2013).
681 2. Kobayashi, Y. *et al.* Persistence of a regeneration-associated, transitional alveolar epithelial cell
682 state in pulmonary fibrosis. *Nat. Cell Biol.* **22**, 934–946 (2020).
683 3. Choi, J. *et al.* Inflammatory Signals Induce AT2 Cell-Derived Damage-Associated Transient
684 Progenitors that Mediate Alveolar Regeneration. *Cell Stem Cell* **27**, 366–382.e7 (2020).
685 4. Strunz, M. *et al.* Alveolar regeneration through a Krt8+ transitional stem cell state that persists
686 in human lung fibrosis. *Nat. Commun.* **11**, 3559 (2020).
687 5. Lehmann, M. *et al.* Senolytic drugs target alveolar epithelial cell function and attenuate
688 experimental lung fibrosis ex vivo. *Eur. Respir. J.* **50**, (2017).
689 6. Kathiriya, J. J., Brumwell, A. N., Jackson, J. R., Tang, X. & Chapman, H. A. Distinct Airway
690 Epithelial Stem Cells Hide among Club Cells but Mobilize to Promote Alveolar Regeneration. *Cell*
691 *Stem Cell* **26**, 346–358.e4 (2020).
692 7. Basil, M. C. *et al.* Human distal airways contain a multipotent secretory cell that can regenerate
693 alveoli. *Nature* **604**, 120–126 (2022).
694 8. Calabrese, F. *et al.* Marked alveolar apoptosis/proliferation imbalance in end-stage emphysema.
695 *Respir. Res.* **6**, 14 (2005).
696 9. Tsuji, T., Aoshiba, K. & Nagai, A. Alveolar cell senescence in patients with pulmonary
697 emphysema. *Am. J. Respir. Crit. Care Med.* **174**, 886–893 (2006).
698 10. Alder, J. K. *et al.* Telomere dysfunction causes alveolar stem cell failure. *Proc. Natl. Acad. Sci.*
699 **112**, 5099–5104 (2015).
700 11. Zysman, M. *et al.* Targeting p16INK4a Promotes Lipofibroblasts and Alveolar Regeneration
701 After Early Life Injury. *Am. J. Respir. Crit. Care Med.* **202**(8):1088-1104 (2020).
702 12. Kohonen, T. & Somervuo, P. How to make large self-organizing maps for nonvectorial data.
703 *Neural Netw.* **15**, 945–952 (2002).
704 13. Wang, Z. *et al.* Optimal Threshold in CT Quantification of Emphysema. *Eur. Radiol.* **23**, 975
705 (2012).
706 14. Gote-Schniering, J. *et al.* Single cell decomposition of multicellular aging programs associated
707 with impaired lung regeneration. *bioRxiv* 2025.07.24.666371 (2025).
708 15. Wang, Z. *et al.* Enhanced glycolysis-mediated energy production in alveolar stem cells is
709 required for alveolar regeneration. *Cell Stem Cell* **30**, 1028–1042.e7 (2023).
710 16. Wang, F. *et al.* Regulation of epithelial transitional states in murine and human pulmonary
711 fibrosis. *J. Clin. Invest.* **133**, (2023).
712 17. Mereu, E. *et al.* Benchmarking single-cell RNA-sequencing protocols for cell atlas projects.
713 *Nat. Biotechnol.* **38**, 747–755 (2020).
714 18. Conlon, T. M. *et al.* Inhibition of LTβR signalling activates WNT-induced regeneration in lung.
715 *Nature* **588**, 151–156 (2020).
716 19. Watanabe, N. *et al.* Anomalous Epithelial Variations and Ectopic Inflammatory Response in
717 Chronic Obstructive Pulmonary Disease. *Am. J. Respir. Cell Mol. Biol.* **67**, 708–719 (2022).
718 20. Hu, Y. *et al.* Airway-derived emphysema-specific alveolar type II cells exhibit impaired
719 regenerative potential in COPD. *Eur. Respir. J.* **64**, (2024).
720 21. Katsura, H., Kobayashi, Y., Tata, P. R. & Hogan, B. L. M. IL-1 and TNFα Contribute to the
721 Inflammatory Niche to Enhance Alveolar Regeneration. *Stem Cell Rep.* **12**, 657–666 (2019).
722 22. Glisinski, K. M. *et al.* Interleukin-13 disrupts type 2 pneumocyte stem cell activity. *JCI Insight*
723 **5**, (2021).

23. Wang, C. *et al.* Dysregulated lung stroma drives emphysema exacerbation by potentiating resident lymphocytes to suppress an epithelial stem cell reservoir. *Immunity* **56**, 576–591.e10 (2023).
24. DiGiovanni, G. T. *et al.* Epithelial Yap/Taz are required for functional alveolar regeneration following acute lung injury. *JCI Insight* **8**, (2023).
25. Cardenas-Diaz, F. L. *et al.* Temporal and spatial staging of lung alveolar regeneration is determined by the grainyhead transcription factor Tfcp2l1. *Cell Rep.* **42**, 112451 (2023).
26. Saul, D. *et al.* A new gene set identifies senescent cells and predicts senescence-associated pathways across tissues. *Nat. Commun.* **13**, 1–15 (2022).
27. Konkimalla, A. *et al.* Transitional cell states sculpt tissue topology during lung regeneration. *Cell Stem Cell* **30**, 1486–1502.e9 (2023).
28. Gote-Schniering, J. & Schiller, H. B. Multilineage circuits of regenerative cell states. *Cell Stem Cell* **30**, 1397–1399 (2023).
29. Crosby, L. M. & Waters, C. M. Epithelial repair mechanisms in the lung. *Am. J. Physiol.-Lung Cell. Mol. Physiol.* **298**, L715–L731 (2010).
30. Dupont, S. *et al.* Role of YAP/TAZ in mechanotransduction. *Nature* **474**, 179–183 (2011).
31. Shiraishi, K. *et al.* Biophysical forces mediated by respiration maintain lung alveolar epithelial cell fate. *Cell* **186**, 1478–1492.e15 (2023).
32. Wu, H. *et al.* Progressive Pulmonary Fibrosis Is Caused by Elevated Mechanical Tension on Alveolar Stem Cells. *Cell* **180**, 107–121.e17 (2020).
33. Amsellem, V. *et al.* Telomere dysfunction causes sustained inflammation in chronic obstructive pulmonary disease. *Am. J. Respir. Crit. Care Med.* **184**, 1358–1366 (2011).
34. Houssaini, A. *et al.* mTOR pathway activation drives lung cell senescence and emphysema. *JCI Insight* **3**, (2018).
35. Krimpenfort, P., Quon, K. C., Mooi, W. J., Loonstra, A. & Berns, A. Loss of p16Ink4a confers susceptibility to metastatic melanoma in mice. *Nature* **413**, 83–86 (2001).
36. Knudsen, L., Weibel, E. R., Gundersen, H. J. G., Weinstein, F. V. & Ochs, M. Assessment of air space size characteristics by intercept (chord) measurement: an accurate and efficient stereological approach. *J. Appl. Physiol.* **108**(2) :412-21 (2010).
37. Belgacemi, R. *et al.* Complex urban atmosphere alters alveolar stem cells niche properties and drives lung fibrosis. *Am. J. Physiol.-Lung Cell. Mol. Physiol.* **325**, L447–L459 (2023).
38. Wolock, S. L., Lopez, R. & Klein, A. M. Scrublet: Computational Identification of Cell Doublets in Single-Cell Transcriptomic Data. *Cell Syst.* **8**, 281–291.e9 (2019).
39. Young, M. D. & Behjati, S. SoupX removes ambient RNA contamination from droplet-based single-cell RNA sequencing data. *GigaScience* **9**, (2020).
40. Coppé, J.-P. *et al.* A Human-Like Senescence-Associated Secretory Phenotype Is Conserved in Mouse Cells Dependent on Physiological Oxygen. *PLOS ONE* **5**, e9188 (2010).
41. Lang J, N. *et al.* Ex vivo tissue perturbations coupled to single-cell RNA-seq reveal multilineage cell circuit dynamics in human lung fibrogenesis. *Sci. Transl. Med.* **15**(725):eadh0908 (2023).
42. Yu, G., Wang, L.-G., Han, Y. & He, Q.-Y. clusterProfiler: an R Package for Comparing Biological Themes Among Gene Clusters. *OMICS J. Integr. Biol.* **16**, 284 (2012).
43. Gao, S., Mutter, S., Casey, A. & Mäkinen, V.-P. Numero: a statistical framework to define multivariable subgroups in complex population-based datasets. *Int. J. Epidemiol.* **48**, 369–374 (2019).
44. Chavent, M., Kuentz-Simonet, V., Labenne, A. & Saracco, J. Multivariate Analysis of Mixed Data: The R Package PCAmixdata. *arXiv.org* https://arxiv.org/abs/1411.4911v5 (2014).

770 **Author contributions**

771 Conceptualization: BRB, MT, GT, MZ, CTDM, SL, JB, JGS, LB

772 Methodology: BRB, MT, GT, PAA, TDFC, MZ, CTDM, EA, MA, KS, HW, ML, JYT, JB,
773 JGS, LB

774 Validation: BRB, MT, SL, FC, CJLS, YH, MK, ML, JYT, GD, JB, JGS, LB

775 Formal analysis: BRB, MT, GT, PAA, TDFC, MZ, EA, CJLS, YH, MK, ML, GD, JB, JGS,
776 LB

777 Investigation: BRB, MT, GT, PAA, TDFC, MZ, CTDM, EA, MA, KS, HW, ML, JGS, LB

778 Data curation: BRB, MT, GT, JGS, LB

779 Supervision: SL, FC, CJLS, ML, JYT, GD, JB, JGS, LB

780 Funding acquisition: BRB, MT, MZ, FC, GD, JB, LB

781 Writing—original draft: BRB, MT, CJLS, JGS, LB

782

Data availability

Single cell RNA-Seq date was submitted to the NCBI GEO database. All code used for data visualization of the scRNA-seq may be requested from the authors upon reasonable request.

Acknowledgment

This work was supported by a fellowship from INSERM and ARAIRLOR (BRB), UPEC doctoral school (MT), IMRB and Oxyvie (LB), Fondation pour la Recherche Medicale (FRM, LB) and Fondation du Souffle (LB). The authors thank members of Team Derumeaux and Team Lanone for their precious expertise and their help, Fanny Coulpier (Institut Mondor de Recherche Biomédicale, IMRB-INSERM U955) for her assistance in performing the single cell analysis, Denis Mestivier for bioinformatic support (Université Paris Est, Créteil, France), Denis Debrosse (APHP, Service de chirurgie thoracique et vasculaire, Hôpital Tenon, Paris, France) for surgical lung tissues, Slimani Lofti from Université de Paris, URP2496 Pathologies, Imagerie et Biothérapies Orofaciales et Plateforme Imagerie du Vivant (PIV) for CT scan images. The authors also thank Xavier Decrouy, Christelle Micheli (IMRB–INSERM U955, Créteil, France) and Adrien Lalot (animal facility). The assistance of Adeline Henry, Odile Ruckebusch and Aurélie Guguin (Installation de Cytométrie en Flux, IMRB-INSERM U955, Créteil, France). We sincerely thank William J. Zacharias (Cincinnati Children's Hospital) for his insightful guidance and generous advice regarding organoid generation. Finally, the authors thank Silvia Fre, Bruno Crestani, Philippos Mourikis and for their advice. The Interfaculty Bioinformatics Unit (IBU), University of Bern provided computational infrastructure and support with bioinformatic analyses. We sincerely thank Matthias Brunner for technical assistance.

Competing interests

The authors declare no competing interests.

Supplementary Figures

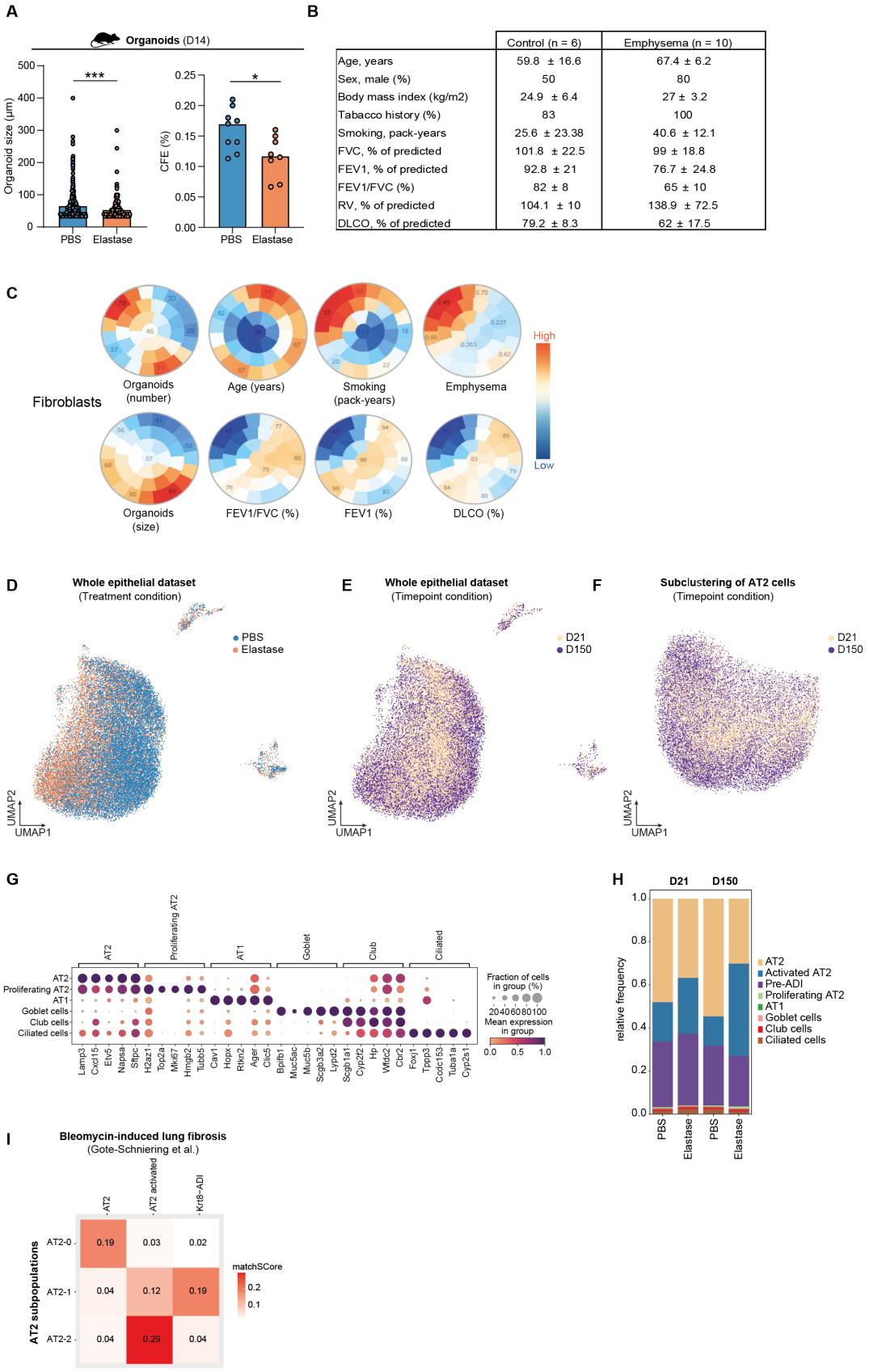

	Control (n = 6)	Emphysema (n = 10)
Age, years	59.8 ± 16.6	67.4 ± 6.2
Sex, male (%)	50	80
Body mass index (kg/m2)	24.9 ± 6.4	27 ± 3.2
Tabacco history (%)	83	100
Smoking, pack-years	25.6 ± 23.38	40.6 ± 12.1
FVC, % of predicted	101.8 ± 22.5	99 ± 18.8
FEV1, % of predicted	92.8 ± 21	76.7 ± 24.8
FEV1/FVC (%)	82 ± 8	65 ± 10
RV, % of predicted	104.1 ± 10	138.9 ± 72.5
DLCO, % of predicted	79.2 ± 8.3	62 ± 17.5

Figure S1: Fibroblasts, epithelial dysfunction, and accumulation of activated AT2 in mouse emphysema (A) Size (µm) and colony forming efficiency (CFE %) of organoids

817 obtained from the coculture of WT EpCAM$^+$ cells obtained by magnetic sorting from elastase
818 and PBS treated mice and WT fibroblasts after 14 days of culture (mean is shown, N = 8/group,
819 n > 200 organoids/group, Mann-Whitney test). (B) Characteristics of patients from whom AT2
820 cells were used to generate organoids. (C) Exploratory unsupervised analysis of the number
821 and size of organoids formed, patient age, smoking history (in pack-years), proportion of
822 emphysema as quantified by chest computed tomography, FEV_1/FVC ratio (%) and FEV_1
823 regarding fibroblasts origins. Color intensity reflects the standardized (z-score) value of each
824 variable, allowing visual comparison across patient subgroups. (D-E) UMAP of 31,172 lung
825 epithelial cells from WT mice treated with PBS or elastase depending on treatment and time
826 point condition. (F) UMAP of 29,941 AT2 cells depending on timepoint condition. (G) Dotplot
827 showing marker gene signatures of the entire epithelial dataset. Scaled mean expression is
828 shown. (H) Relative frequencies of cell types/states within the entire epithelium dataset
829 stratified by treatment and time point condition. (I) MatchScore between AT2 subpopulations
830 of our dataset compared with[14]. *p = 0.05, **p = 0.01, ***p = 0.001, ****p = 0.0001 and ns
831 = not significant

832

833

834

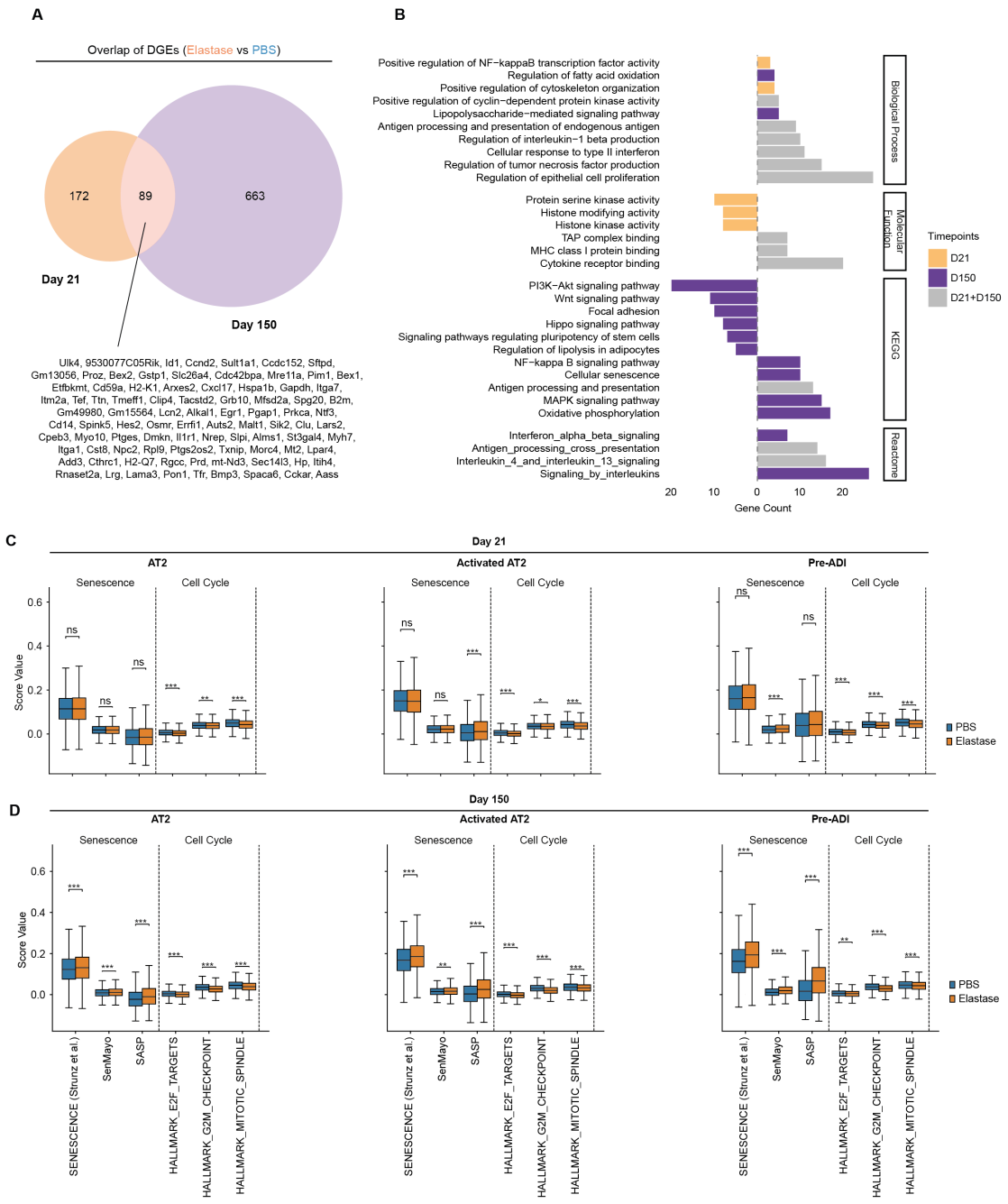

Figure S2: Pathway, senescence, and cell cycle in alveolar epithelial cells in elastase-induced emphysema (A) Venn diagram showing the overlap of differentially expressed genes (log fold change >0.25, q-value < 0.05) between elastase and PBS-treated AT2 from WT animals at D21 and D150 post-treatment. (B) Representative results of the GO and pathway enrichment analysis stratified by time point and pathway category comparing AT2 from WT mice treated with elastase or PBS. The color code indicates differential regulation at D21, D150 or at both time points (D21+D150). (C-D) Boxplots showing the senescence and cell cycle

844 scoring results across the three AT2 subpopulations at D21 and D150. Statistics: Mann-
845 Withney U test.

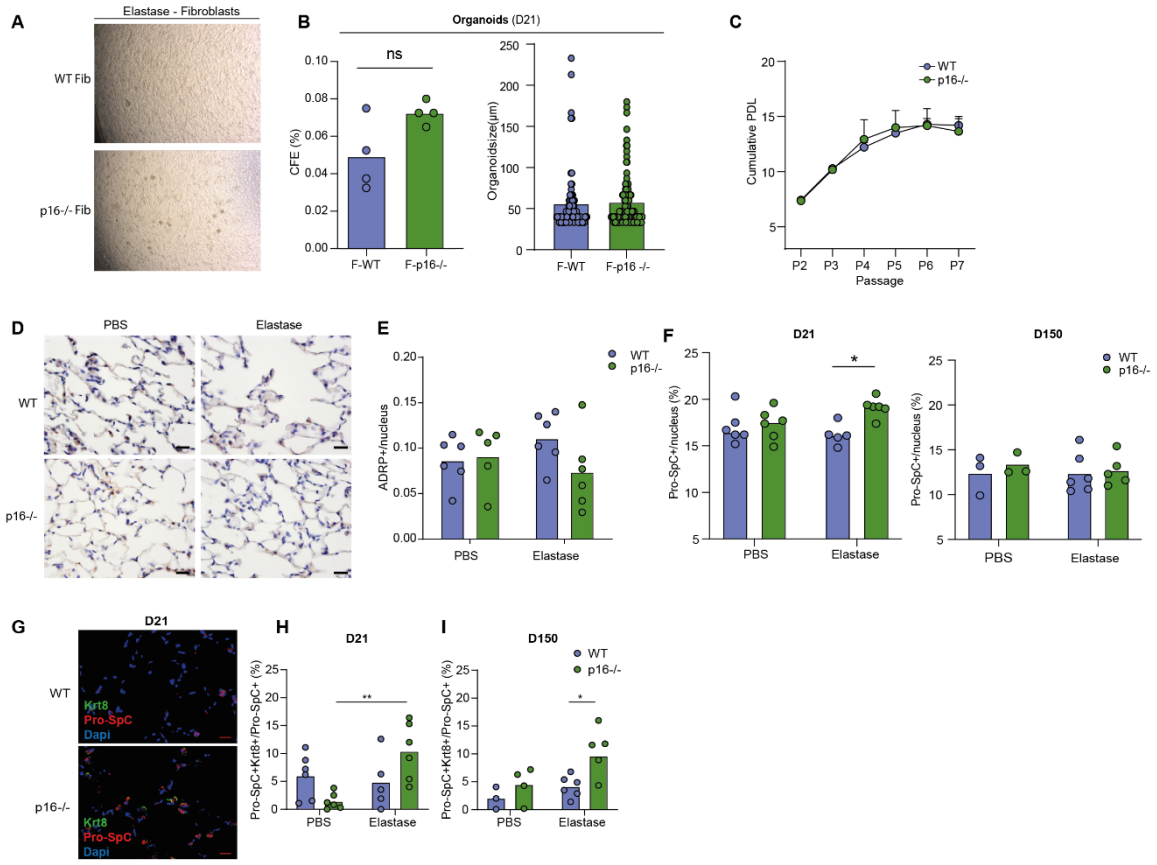

846

847 **Figure S3: Fibroblasts and pre-ADI in elastase WT and p16$^{-/-}$ mice** (A) Representative
848 images of organoids obtained from the coculture of WT or p16$^{-/-}$ fibroblasts (F-WT and F-p16^{-}
849 $^{/-}$) treated with elastase and WT-EpCAM^{+} cells also treated with elastase (scale bar = 20 µm)
850 (B) Colony forming efficiency (CFE %) and size (µm) of organoids WT or p16$^{-/-}$ treated with
851 elastase (mean is shown, N = 4/group, n > 50 organoids/group, Mann-Whitney test). (C)
852 Cumulative population doubling level (PDL) of fibroblasts from lungs of WT or p16$^{-/-}$ mice
853 from passage 2 (P2) to passage 7 (P7) (n = 3 biological replicates, Error bars indicate the SEM).
854 (D) Immunohistochemistry of lipofibroblasts by adipose differentiation-related protein
855 (ADRP) staining on lungs of WT and p16$^{-/-}$ mice instilled with PBS or elastase (scale bar = 20
856 µm). (E) Quantification of the number of lipofibroblasts at D90 post-treatment (mean is shown,
857 N = 6, two-way ANOVA test). (F) Quantification of the number of AT2 cells among all cells
858 in WT and p16$^{-/-}$ mice at D21 and D150 (mean is shown, N > 3, two-way ANOVA test). (G)
859 Immunofluorescence of Pro-SpC (red) and KRT8 (green) in WT and p16-/- mice at D21 (scale
860 bar = 20 µm). (H,I) Quantification of the number of Pro-SpC+/KRT8+ among AT2 cells (Pro-

SpC+) at D21 (H) and D150 (I) post PBS or elastase treatment in lungs of WT and p16-/- mice (mean is shown, N = 3-6, two-way ANOVA test).

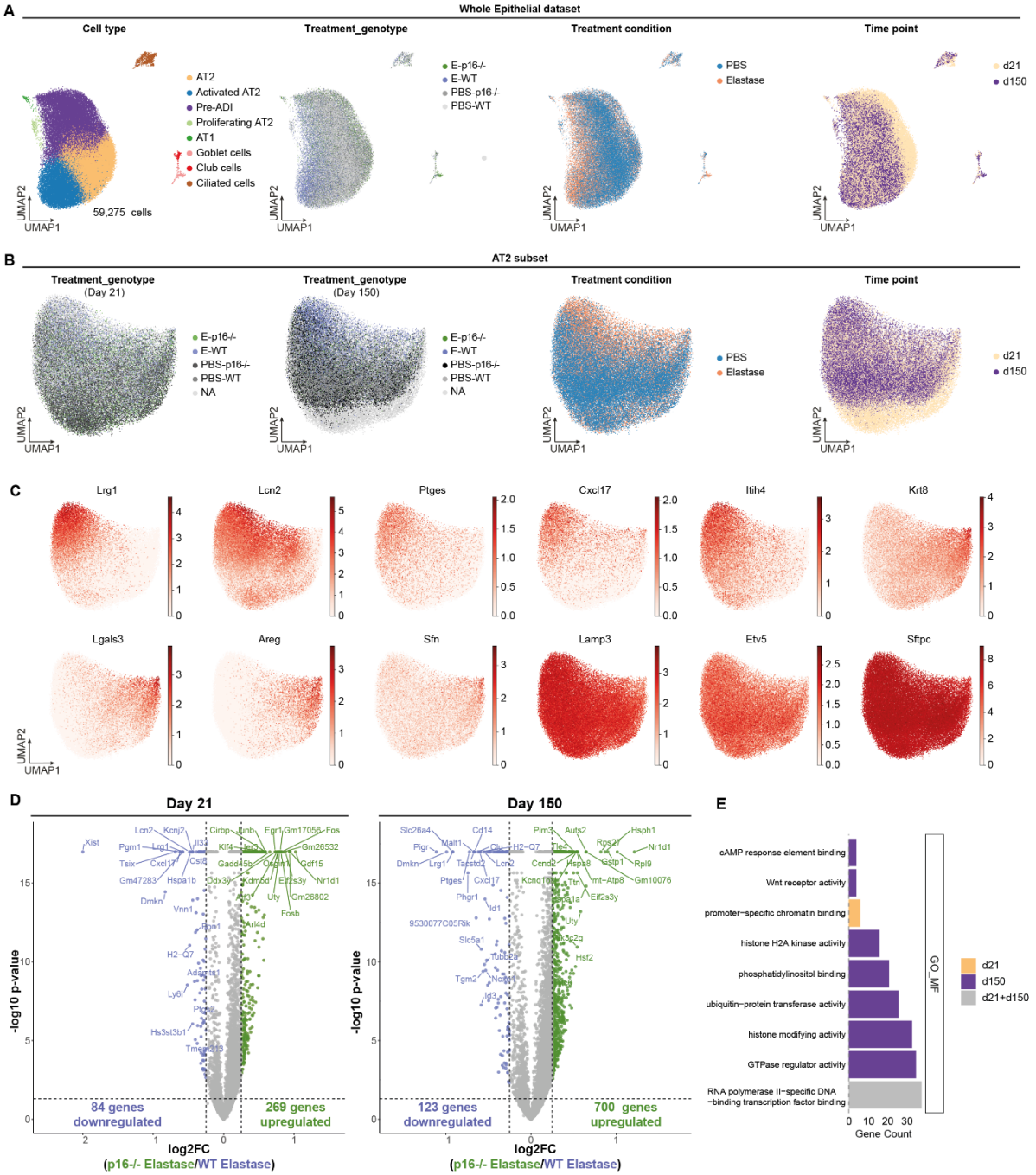

Figure S4: Single-cell RNA-seq of epithelial cells from WT and p16-/- deficient mice treated with PBS or elastase. (A) UMAP of 59,172 lung epithelial cells from WT and p16-/- deficient mice treated with PBS or elastase depending on treatment, genotype and timepoint conditions. (B) UMAP of 57,779 AT2 cells depending on treatment, genotype and timepoint condition. (C) UMAP feature plots highlighting the expression of selected marker genes for

activated AT2 (*Lrg1, Lcn2, Ptges, Cxcl17, Itih4*), pre-ADI (*Krt8, Lgals3, Areg, Sfn*), and canonical AT2 (L*amp3, Etv5, Sftpc*). (D) Volcano plots of differentially expressed genes at D21 and D150 in AT2 cells of elastase-treated p16$^{-/-}$ mice compared to elastase-treated WT mice. A log fold change of 0.25 and q-value of less than 0.05 was used to define differential expressions. Upregulated genes in the knockout condition are shown in green, downregulated genes in blue, and non-significant genes in grey. (E) Results of GO Molecular function enrichment analysis stratified by time point and pathway category comparing AT2 cells of elastase-treated p16-/- mice compared to elastase-treated WT mice. The color code indicates differential regulation at D21, D150 or at both time points (D21+D150).

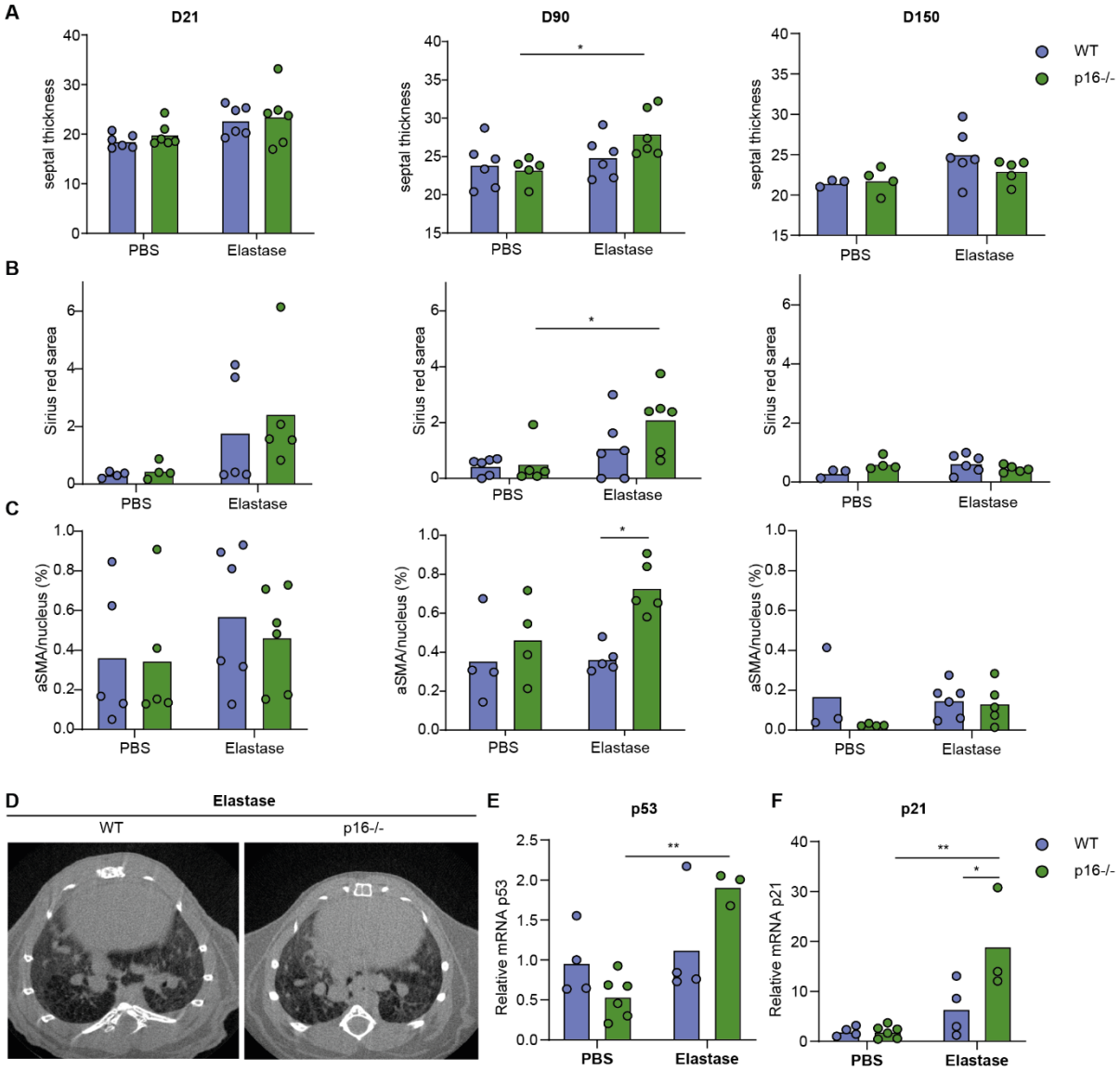

Figure S5: p16 deletion induces lung regeneration without aberrant process of lung fibrosis (A) Septal thickness of the alveolar wall, (B) Sirius red area and (C) myofibroblasts

881 (αSMA) quantifications at D21, D90 and D150 in WT or p16$^{-/-}$ mice instilled with PBS or
882 elastase (mean is shown, N = 6/group, two-way ANOVA test). (D) Lung CT scan of WT and
883 p16$^{-/-}$ mice 12 months after elastase treatment. (E-F) Relative mRNA quantification of p53 (E)
884 and p21 (F) by RT-qPCR performed 21 days after instillation with PBS or elastase of WT or
885 p16$^{-/-}$ mice (mean is shown, N = 3/group, two-way ANOVA test). *p = 0.05, **p = 0.01, ***p
886 = 0.001, ****p = 0.0001 and ns = not significant

887

888

889